

3D Simulations of the Early Martian Hydrological Cycle Mediated by a H₂-CO₂ Greenhouse

Scott D. Guzewich¹, Michael Way², Igor Aleinov³, Eric T Wolf⁴, Anthony D. Del Genio⁵, Robin Wordsworth⁶, and Kostas Tsigaridis⁷

¹NASA Goddard Spaceflight Center

²NASA/Goddard Institute for Space Studies

³Columbia University

⁴University of Colorado Boulder

⁵National Aeronautics and Space Administration (NASA)

⁶Harvard University

⁷Center for Climate Systems Research, Columbia University, and NASA Goddard Institute for Space Studies

November 21, 2022

Abstract

For decades the scientific community has been trying to reconcile abundant evidence for fluvial activity on Noachian and early Hesperian Mars with the faint young Sun and reasonable constraints on ancient atmospheric pressure and composition. Recently, the investigation of H₂-CO₂ collision induced absorption has opened up a new avenue to warm Noachian Mars. We use the ROCKE-3D global climate model to simulate plausible states of the ancient Martian climate with this absorptive warming and reasonable constraints on surface paleopressure. We find that 1.5-2 bar CO₂-dominated atmospheres with 3% H₂ can produce global mean surface temperatures above freezing, while also providing sufficient warming to avoid surface atmospheric CO₂ condensation at 0°-45° obliquity. Simulations conducted with both modern topography and a paleotopography, before Tharsis formed, highlight the importance of Tharsis as a cold trap for water on the planet. Additionally, we find that low obliquity (modern and 0°) is more conducive to rainfall over valley network locations than high (45°) obliquity.

3D Simulations of the Early Martian Hydrological Cycle Mediated by a H₂-CO₂ Greenhouse

Scott D. Guzewich, Michael Way, Igor Aleinov, Eric T. Wolf, Anthony Del Genio, Robin Wordsworth, Kostas Tsigaridis

ABSTRACT

For decades the scientific community has been trying to reconcile abundant evidence for fluvial activity on Noachian and early Hesperian Mars with the faint young Sun and reasonable constraints on ancient atmospheric pressure and composition. Recently, the investigation of H₂-CO₂ collision-induced absorption has opened up a new avenue to warm Noachian Mars. We use the ROCKE-3D global climate model to simulate plausible states of the ancient Martian climate with this absorptive warming and reasonable constraints on surface paleopressure. We find that 1.5-2 bar CO₂-dominated atmospheres with $\geq 3\%$ H₂ can produce global mean surface temperatures above freezing, while also providing sufficient warming to avoid surface atmospheric CO₂ condensation at 0°-45° obliquity. Simulations conducted with both modern topography and a paleotopography, before Tharsis formed, highlight the importance of Tharsis as a cold trap for water on the planet. Additionally, we find that low obliquity (modern and 0°) is more conducive to rainfall over valley network locations than high (45°) obliquity.

1. INTRODUCTION

2

3 Abundant geologic evidence strongly implies that surface liquid water was widespread on
4 ancient Mars approximately 3.5-4 billion years ago, in the time period termed the Noachian. Such
5 evidence includes riverine channels (e.g., Masursky, 1973; Pieri, 1980; Hynek and Phillips, 2001;
6 Hynek et al., 2010), craters filled with sedimentary deposits and including inflow and outflow
7 channels (e.g., Irwin et al., 2005; Fasset and Head, 2005; Schon et al., 2012), minerals that only

8 form in the presence of liquid water (e.g., Murchie et al., 2009; Ehlmann et al., 2011; Carter et al.,
9 2013), and features implying aqueous erosion (e.g., Carr, 1996; Malin and Edgett, 2000).

10 Work to deduce what climatic conditions were possible to produce such geologic evidence
11 has been ongoing for decades and Wordsworth (2016) provides a recent review of the state of
12 knowledge. One-dimensional radiative-convective models were initially used (e.g., Pollack, 1979;
13 Pollack et al., 1987) and habitable conditions (typically defined as global mean surface
14 temperatures above 273 K) were generated with sufficiently large surface air pressures of CO₂-
15 dominated atmospheres, even with the ~25% dimmer young Sun, although not in all models (e.g.,
16 Postawko and Kuhn, 1986). Kasting (1991) showed that CO₂-H₂O atmospheres alone were
17 insufficient to warm ancient Mars due to increased Rayleigh scattering at high pressure and CO₂
18 ice condensation on the surface. Increasing sophistication of the models (e.g., incorporation of
19 cloud effects) over time and doubts about the plausibility of very thick (>2 bar) atmospheres made
20 reconciling the geologic evidence challenging. A plethora of greenhouse mixtures (CH₄, NH₃,
21 SO₂, cirrus clouds, and others) have been proposed, but all have unique problems being retained
22 in a putative ancient atmosphere (e.g., Kuhn and Atreya, 1979; Kasting, 1997; Tian et al., 2010;
23 Urata and Toon, 2013; Mischna et al., 2015; Kerber et al., 2015; Turbet et al. 2020a). More
24 recently, indirect evidence (e.g., crater counting statistics) has implied that the ancient martian
25 atmospheric pressure was likely less than 1 bar, with perhaps 2 bar being consistent with the data,
26 at least for geologically short time periods (Cassata et al., 2012; Manga et al., 2012; Kite et al.,
27 2014; Warren et al., 2019).

28 Limiting ancient martian atmospheric pressure to terrestrial-comparable levels in
29 combination with the Faint Young Sun presents a strong challenge to long-term (i.e., tens to
30 hundreds of millions of years) “warm and wet” conditions. More punctuated and brief warm

31 climate periods interspersed with cold and dry conditions (perhaps with seasonal melting) also
32 may fit some of the geologic evidence while also being consistent with Mars general circulation
33 models (Fastook et al., 2012; Wordsworth et al., 2013; Fastook and Head, 2015; Cassenelli and
34 Head, 2015; Wordsworth et al., 2015). Yet, some geologic evidence (e.g., Williams et al., 2013,
35 Grant et al., 2014; Grotzinger et al., 2014; Kite et al., 2017) still requires some persistent duration
36 of warm and wet conditions. Recently, H₂ has been offered as another possible greenhouse gas
37 (Wordsworth and Pierrehumbert, 2013; Ramirez et al., 2014). Importantly, collision-induced
38 absorption (CIA) between H₂ and CO₂ has been shown to be efficacious at generating considerable
39 warming through *ab initio* calculations (Wordsworth et al., 2017) and experiments (Turbet et al.,
40 2019, 2020; Godin et al., 2020; Mondelain et al., 2021), although the experimental results
41 demonstrate slightly more modest absorption than the *ab initio* calculations.

42 One-dimensional climate models including CIA between H₂, CO₂, and CH₄ generate global
43 mean surface temperatures above the freezing point of water for reasonable atmospheric pressures
44 during the Noachian period (Ramirez et al., 2014; Batalha et al., 2015; Wordsworth et al., 2017;
45 Hayworth et al., 2020). Three-dimensional general circulation models (GCMs) have also begun
46 experiments including such CIA absorption (Haberle et al., 2019; Kamada et al., 2020). One
47 challenge that remains however, is retaining comparatively large partial pressures of H₂, which
48 should have escaped rapidly during a time period when the Sun was more active (e.g., Jakosky et
49 al., 2018). Ramirez et al. (2014) suggested the martian mantle may be more reduced and thus emit
50 more H₂ relative to Earth, while still producing CO₂ through chemical processes in the atmosphere
51 (see Hirschmann and Withers (2008) which imply reduced CO₂ outgassing from a reduced mantle).
52 Water-rock chemical reactions (particularly with iron-bearing materials) could have generated
53 substantial H₂ fluxes (Hurowitz et al., 2010; Tarnas et al., 2018; Tosca et al., 2018). Haberle et al.

54 (2019) suggests that iron-rich meteorites impacting Mars would have degassed abundant H₂,
55 creating large H₂ partial pressures for short durations (up to 10⁴ years for 100 km sized objects)
56 following the impact.

57 In this work, we examine two science questions related to the early martian climate:

- 58 1. What range of atmospheric pressure and greenhouse gas mixtures can
59 permit global mean annual surface temperatures above the freezing point of
60 water?
- 61 2. What is the fate of liquid water on the surface of ancient Mars?

62 We have performed a range of GCM simulations with the Resolving Orbital and Climate Keys of
63 Earth and Extraterrestrial Environments with Dynamics 1.0 (ROCKE-3D) general circulation
64 model to study these questions. Our radiative transfer model employs the CIA absorption as
65 described by Wordsworth et al. (2017) and is flexible enough to allow varying surface pressures,
66 gas mixtures, and global water inventories. In Section 2 we describe our methodologies and the
67 radiative transfer scheme in detail. In Section 3 we present and discuss our results. Finally, in
68 Section 4 we conclude.

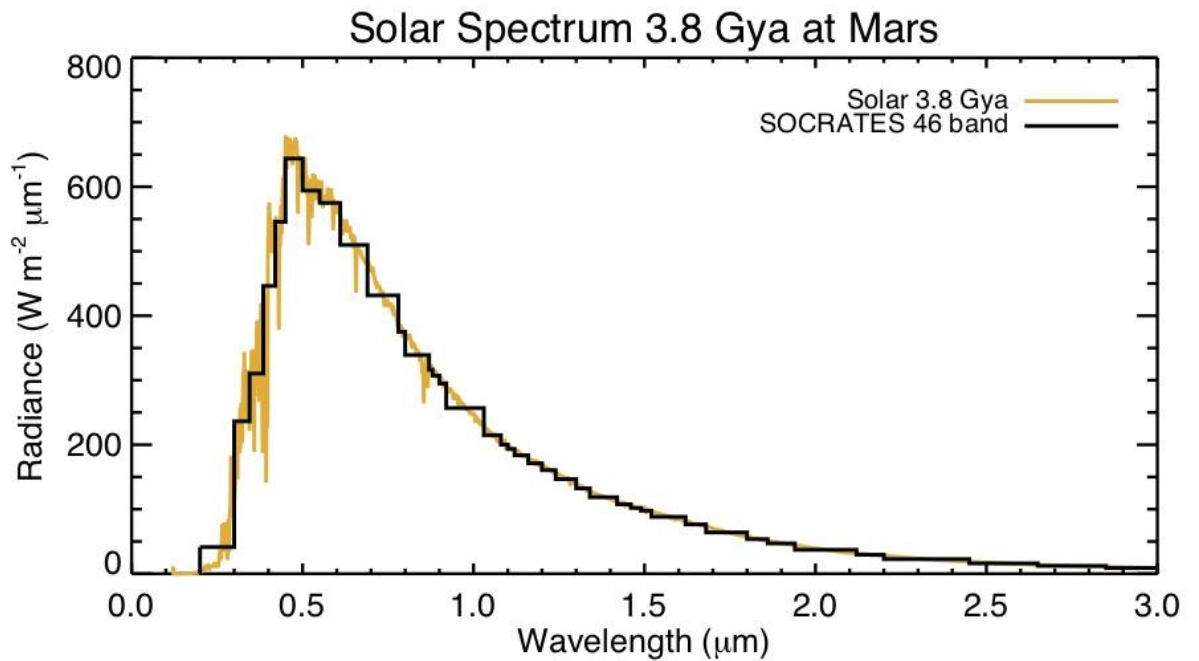
69 2. METHODOLOGY

70 We employ the ROCKE-3D GCM for our simulations. Way et al. (2017) describes the
71 broad capabilities of ROCKE-3D to simulate rocky planet atmospheres both in and out of the Solar
72 System. Within the Solar System, ROCKE-3D has been used to study possible paleo-
73 environments of early Venus (Way et al., 2016; Way and Del Genio, 2020) and transient
74 atmospheres on Earth's moon (Aleinov et al., 2019). ROCKE-3D is freely available for download
75 at <https://simplex.giss.nasa.gov/gcm/ROCKE-3D/> and instructions for setup and testing are
76 provided.
77
78

79 ROCKE-3D has heritage from the NASA Goddard Institute for Space Studies ModelE2
80 and employs many facets of that terrestrial climate model, including the dynamical core and many
81 physical parameterizations (e.g., water ice cloud physics, surface and subsurface runoff, ocean
82 dynamics, etc.). As a GCM designed to simulate hypothetical exoplanet environments and ancient
83 conditions in our Solar System, several modifications were required in the transition from
84 ModelE2 to ROCKE-3D. First among these is the adoption of the Suite of Community Radiative
85 Transfer codes (SOCRATES) radiation scheme [e.g., Amundsen et al., 2016] that is adaptable to
86 non-terrestrial gas mixtures, varying stellar insolation, and stellar type. SOCRATES uses a two-
87 stream radiative transfer solver with correlated-k distributions to solve for shortwave and
88 longwave absorption and scattering [Edwards 1996; Edwards and Slingo, 1996]. SOCRATES
89 can be flexibly configured to suit particular atmospheric gas mixtures, stellar spectrum, and
90 spectral resolutions. Here, SOCRATES has been configured specifically for paleo Mars
91 atmospheres, suitable for multi-bar CO₂ dominated atmospheres, along with H₂O, CH₄, H₂, and
92 N₂ at lesser amounts. Gas absorption is included via the current best practices. CO₂ line absorption
93 is included with a sub-Lorentzian line shape truncated at 500 cm⁻¹ from the line centers. H₂O and
94 CH₄ line absorption assumes a Voigt profile truncated at 25 cm⁻¹ from the line centers. The H₂O
95 self and foreign broadened continua are included using the MT_CKD version 3.0 continuum model
96 (Clough et al. 2005), and collision induced absorption (CIA) for CO₂-CO₂ and other important
97 pairs are also included.

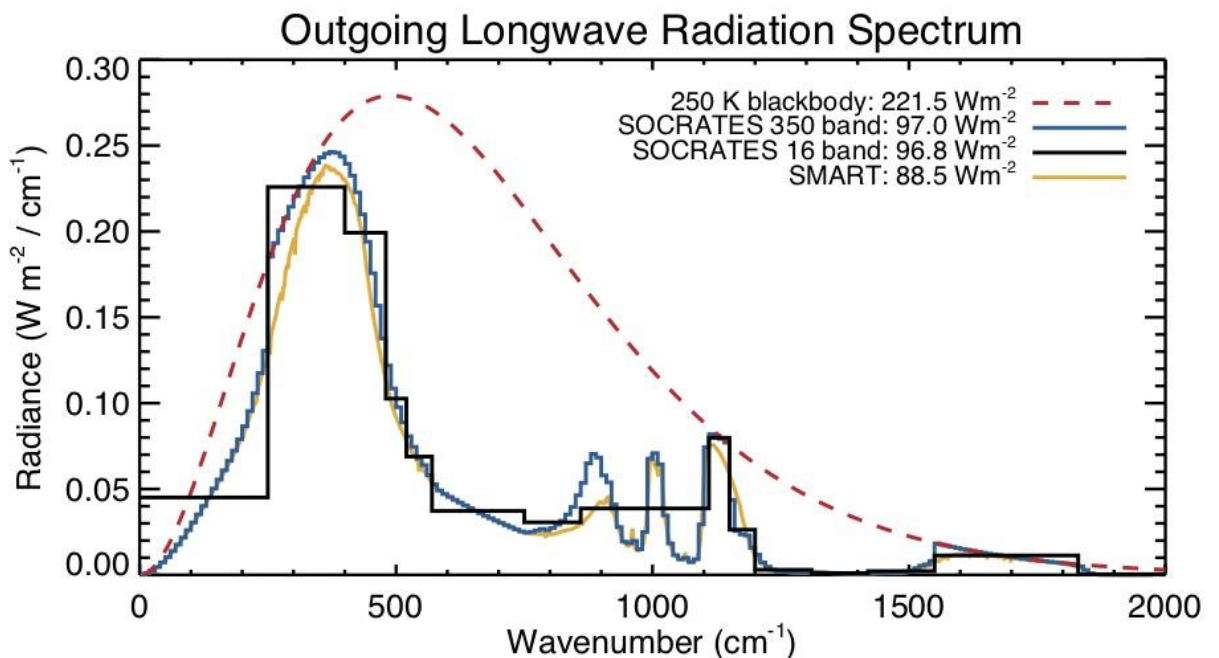
98 Figure 1 shows the input stellar spectrum used in this work, taken as the Sun spectrum at
99 3.8 Ga from Claire et al. (2012) with the spectral scaling calibrated to Lean et al. (1995), and with
100 the total solar flux scaled to Mars at this time period (442 Wm⁻²). Our Sun has slowly brightened
101 over time (Gough, 1981), and at 3.8 Ga the Sun was only ~75% as luminous as it is today. Also,

102 at this time period, the Sun was slightly redder, with an effective temperature of about ~ 100 K
103 cooler than it is today (Claire et al., 2012). The result of the effective temperature change is that
104 slightly more radiation is emitted in the near-infrared compared to the visible, relative to the
105 present-day Sun. In practice, assuming an identical incident stellar flux, the downwelling stellar
106 flux that reaches the surface through a nominal early Mars-like atmosphere is lessened by only a
107 few tenths of Wm^{-2} compared to the using the present-day Sun spectrum. Overlaid on Figure 1
108 are the 46 shortwave bands used in our model. Previous works have shown that adequate
109 shortwave radiative transfer performance requires resolving absorption bands and windows in the
110 near-infrared (Yang et al. 2016). Thus, 46 bands were used to parse out H_2O , CO_2 , and CH_4
111 absorption in this spectral region.



112
113 Figure 1: The stellar spectrum at 3.8 Ga (orange) along with the 46-band
114 discretization of this stellar spectrum used in our SOCRATES shortwave radiative transfer
115 calculation (black).

116 Figure 2 illustrates the longwave performance of our radiative transfer model. Here,
117 duplicating previously published calculations, we assume a 2-bar pure CO₂ atmosphere with a 250
118 K surface temperature, a dry adiabatic lapse rate, and a 167 K isothermal stratosphere. We
119 compare radiative transfer calculations from SOCRATES using the GCM resolution (16 bands), a
120 high-resolution configuration of SOCRATES (350 bands), and also with published calculations
121 using SMART (see Kopparapu et al. 2013, Fig. 1). Our SOCRATES calculations, both with the
122 GCM resolution and high-resolution versions, underestimate CO₂ absorption thus allowing more
123 outgoing longwave radiation (OLR) by $\sim 8 \text{ W m}^{-2}$ compared with SMART calculations at 88.5 W m^{-2}
124 ². Identical calculations conducted by Wordsworth et al. (2010) using a two-stream correlated-k
125 approach indicate an OLR of 88.17 W m^{-2} . However, more recent calculations featured in
126 Wordsworth et al. (2017, supplemental materials), that used a line-by-line multi-stream approach,
127 yielded an OLR of $\sim 92 \text{ W m}^{-2}$. By either comparison, our model features somewhat weaker thermal
128 absorption by CO₂ compared with other published results, meaning that our pure-CO₂ simulations
129 may yield slightly colder surface temperatures than other codes.



130

131 Figure 2: Outgoing longwave radiation spectrum from a 250 K blackbody (red
132 dashed) and from 1-D offline radiative transfer calculations using SOCRATES at high
133 resolution (blue), the GCM resolution (black), and SMART (orange). Here we have
134 assumed a 2-bar CO₂-only atmosphere with a 250 K surface temperature and 167 K
135 isothermal stratosphere. Our model underestimates absorption by a pure-CO₂
136 atmosphere.

137 Note, that here we have used the ab initio CO₂-H₂ and CO₂-CH₄ CIA from Wordsworth et
138 al. (2017). However, recent laboratory work by Turbet et al. (2020b) argues that the Wordsworth
139 CIA's overestimate their greenhouse effect. Further note that Godin et al. (2020) independently
140 conducted laboratory measurements of CO₂-H₂ and CO₂-CH₄ CIAs which are in agreement with
141 those measured by Turbet et al. (2020). To test potential biases, here we have performed off-line
142 calculations with SOCRATES to assess the differences between the Wordsworth et al. (2017) and
143 Turbet et al. (2020b) CIA's. Assuming an atmospheric composition of 90% CO₂, 2% CH₄ or H₂,
144 and N₂ constituting the remainder in a 2-bar atmosphere, we have found that the Wordsworth et
145 al. (2017) CIA's overestimate longwave absorption by ~3 and ~8 Wm⁻² compared to the Turbet et
146 al. (2020b) for CO₂-CH₄ and CO₂-H₂ CIA's respectively. Thus, fortuitously, our model benefits
147 from the cancellation of errors, between an underestimation of absorption by pure CO₂, and an
148 overestimation of absorption by the Wordsworth et al. (2017) CIA's compared to the new
149 laboratory measurements.

150 The surface hydrological cycle is represented by a system of dynamic lakes and a
151 groundwater scheme. The lakes are assumed to have a conical shape, so they change their exposed
152 area depending on the amount of stored water. If the amount of stored water exceeds a pre-defined
153 sill depth, the excess of water is moved to the lake system in a neighbouring cell according to a

154 prescribed river routing scheme. If no river routing is prescribed for a particular cell, the lake is
155 allowed to grow there indefinitely. The ground hydrology part employs a six-layer soil scheme
156 (Abramopoulos et al., 1988; Rosenzweig & Abramopoulos, 1997) with the upper layer being 0.1
157 m deep and the rest growing geometrically with depth up to a total of 3.5 m. The thermal and
158 hydrological properties of each layer are computed according to the prescribed composition of soil
159 components (sand, clay, silt) and present water. The heat between the layers is exchanged
160 according to the thermal conductivity law and can be transported by water. The water can drain
161 to the lower layers due to gravity (according to Darcy's law) or it can be taken to the upper layers
162 by the capillary uplifting. The amount of water in each layer is not allowed to exceed the saturation
163 level or fall below the hygroscopic minimum, which are defined by the local soil texture. The
164 bottom of the lowest layer is assumed to be impermeable to heat and water. Part of the water from
165 each layer can be lost to underground runoff, which is assumed to be proportional to the local slope
166 (prescribed according to the local topography). The upper soil layer can also experience surface
167 runoff, which depends on its level of saturation and the strength of the rain storm. All runoff water
168 is redirected to the local lakes. All heat and water exchange with the atmosphere is performed
169 through the upper layer. The upper layer of soil receives water from precipitation and condensation
170 and loses it through evaporation and runoff. If the precipitation is in a solid form, the ground
171 hydrology algorithm forms a snowpack. The snowpack is represented by a three-layer snow model
172 with its own melting and refreezing cycle. The fraction of the ground covered by snow is defined
173 by the snow thickness and local topography. The lakes can also form lake ice when the amount of
174 heat in the lake falls below the freezing threshold, and they can accumulate snow on top of the ice.
175 The albedo of the surface is defined by the fraction of the lakes, the albedo of the bare soil (which
176 is prescribed for the dry soil, but can decrease when the soil gets wet) and the fraction of ice and

177 the snow. The albedo of the snow depends on the grain size and is assumed to decrease with its
178 age (Hansen et al., 1983).

179 For our ancient Mars simulations discussed in this work, we run the model at 4° latitude
180 by 5° longitude resolution with 40 vertical atmospheric layers from the surface (500-2000 mb) to
181 ~0.1 mb at the top. Mars orbital parameters use modern values except for specific simulations
182 where obliquity is changed as discussed below. Similarly, we use modern Mars topography for
183 simplicity in most simulations and initialize the surface as having uniform 15% broadband albedo
184 with sandy soil. It's reasonable to assume that the Noachian surface could have been darker than
185 the modern due to less surface oxidation, although snow and ice cover could have offset that to
186 some degree. Of course the true Noachian surface albedo is unknown, but note this value of 15%
187 is lower than some other Noachian Mars climate simulations, many of which use modern surface
188 albedo distributions (e.g., Forget et al., 2013). Some simulations (detailed below) use a possible
189 paleotopography (Table 1) shown by Bouley et al. (2016) (see also Matsuyama and Manga, 2010)
190 before the development of the Tharsis Montes and associated true polar wander (TPW). All
191 simulations use an “active lakes” capability of ROCKE-3D (also used for ancient Venus by Way
192 et al., 2016) where the model can produce bodies of surface liquid water based on runoff and
193 precipitation patterns. In some simulations, we initialize the model with existing surface liquid
194 water as “lakes” in topographic low points such as Hellas Basin, deep craters, and the northern
195 lowlands. The model simulates an active water cycle with frozen and liquid precipitation,
196 deposition of snow on the surface, and surface runoff. Note the model does not include CO₂ ice
197 in the atmosphere or on the surface, even if the temperature falls below the frost point. Some
198 ancient Mars climate studies have suggested that CO₂ ice clouds may play an important role in
199 warming the planet's surface (Forget and Pierrehumbert, 1997; Forget et al., 2013; Wordsworth et

200 al., 2013). CO₂ cloud physics are in development for ROCKE-3D and their impacts will be
 201 examined in future work.

202 Our simulations are all run until they reach radiative equilibrium. Simulations that are
 203 initialized with “dry” soil (and thus have minimal, but nonzero, global water inventory) are run for
 204 20 Mars years with the final year used for results below. Simulations initialized with “wet” soil
 205 or with surface liquid water are run until they both reach radiative and hydrological equilibrium.
 206 Evaluating hydrological equilibrium is discussed below. In practice, hydrological equilibrium
 207 requires ~500 Mars years of model run time with modern topography and 2000 years or more for
 208 the paleotopography.

209 All our simulations are listed in Table 1. Any gas mixtures that do not sum to 100% include
 210 the remaining percent as N₂. Simulations with initialized surface water are presented as the total
 211 volume (in global equivalent layer, GEL) and whether the water was initialized as lakes or oceans
 212 in the model.

213 Table 1.

Simulation	Surface Pressure (bar)	% CO₂	% H₂	% CH₄	Soil Moisture	Topography	Surface Water	Obliquity
05H0	0.5	89	0	1	Dry	Modern	None	25.19°
05H3	0.5	86	3	1	Dry	Modern	None	25.19°
1H0	1	89	0	1	Dry	Modern	None	25.19°
1H3	1	86	3	1	Dry	Modern	None	25.19°
AK1	1	97	3	0	Dry	Modern	None	25.19°
RW1	1	94	5	1	Dry	Modern	None	25.19°
1H6	1	83	6	1	Dry	Modern	None	25.19°
RH1	1	90	10	0	Dry	Modern	None	25.19°
15H0	1.5	89	0	1	Dry	Modern	None	25.19°

15H3	1.5	86	3	1	Dry	Modern	None	25.19°
15H5	1.5	94	5	1	Dry	Modern	None	25.19°
AK15	1.5	97	3	0	Dry	Modern	None	25.19°
RH15	1.5	90	10	0	Dry	Modern	None	25.19°
2H0	2	89	0	1	Dry	Modern	None	25.19°
2H3	2	86	3	1	Dry	Modern	None	25.19°
AK2	2	97	3	0	Dry	Modern	None	25.19°
RW2	2	94	5	1	Dry	Modern	None	25.19°
RW2wet	2	94	5	1	Wet	Modern	None	25.19°
RH2	2	90	10	0	Dry	Modern	None	25.19°
RW2lakes	2	94	5	1	Wet	Modern	10m GEL Lakes	25.19°
RW2lakeso0	2	94	5	1	Wet	Modern	10m GEL Lakes	0°
RW2lakeso45	2	94	5	1	Wet	Modern	10m GEL Lakes	45°
RW2lakes100	2	94	5	1	Wet	Modern	100m GEL Lakes	25.19°
RW2lakes100o0	2	94	5	1	Wet	Modern	100m GEL Lakes	0°
RW2lakes500	2	94	5	1	Wet	Modern	500m GEL Lakes	25.19°
RW2TPWlakes	2	94	5	1	Wet	Paleo	10m GEL Lakes	25.19°
RW2TPWlakeso0	2	94	5	1	Wet	Paleo	10m GEL Lakes	0°
RW2TPWlakeso45	2	94	5	1	Wet	Paleo	10m GEL Lakes	45°
RW2TPWlakes100	2	94	5	1	Wet	Paleo	100m GEL Lakes	25.19°
RW2TPWlakes100o0	2	94	5	1	Wet	Paleo	100m GEL Lakes	0°

RW2TPWlakes500	2	94	5	1	Wet	Paleo	500m GEL Lakes	25.19°
NHOcean	2	94	5	1	Wet	Modern	Ocean	25.19°
HOcean	2	94	5	1	Wet	Modern	Ocean	25.19°

214

215

216 3. RESULTS

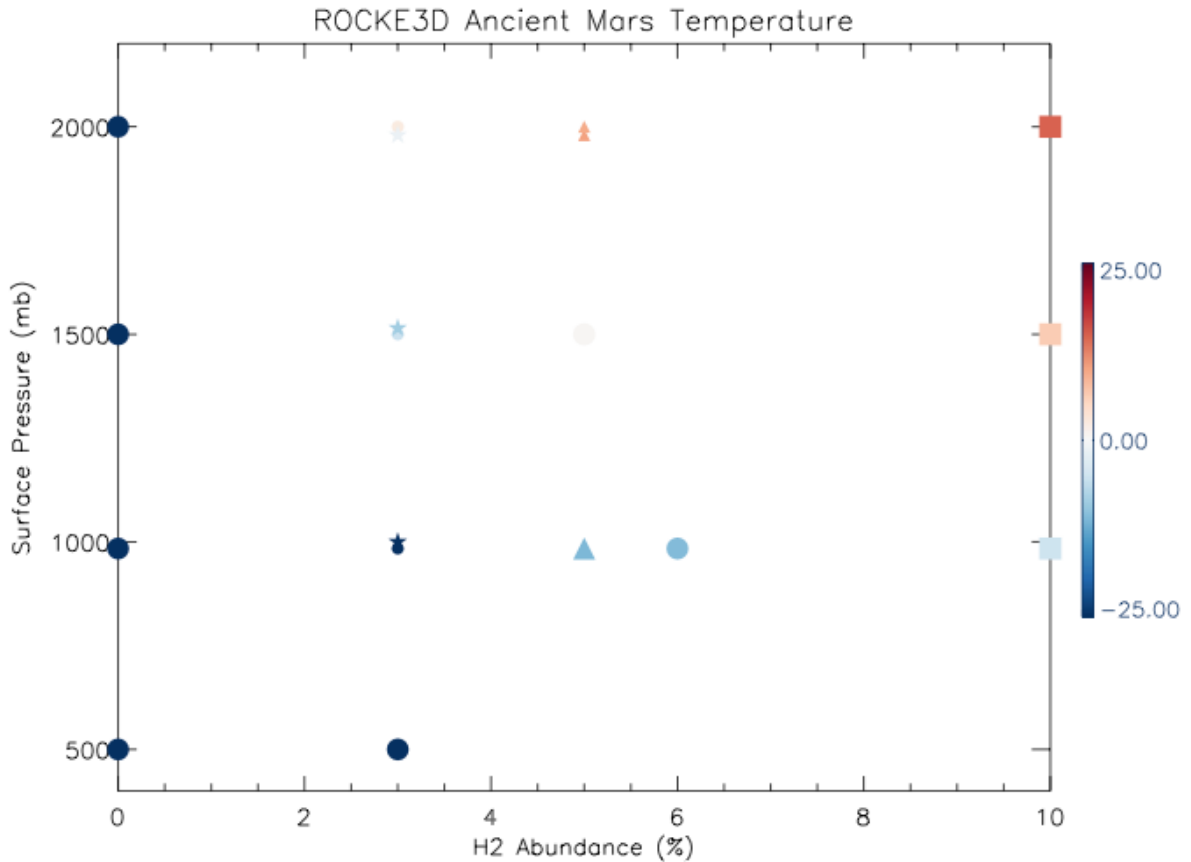
217 We group our simulations into two categories: those initiated with no surface liquid water
 218 and either dry or wet soil and those initiated with some inventory of surface liquid water. We use
 219 the first group, which we generally term as “dry” simulations, to find gas mixtures and surface
 220 pressure values that are supportive of surface liquid water to use in the “wet” simulations (those
 221 initiated with surface liquid water).

222 3.1. Dry Simulations

223 Our dry simulations all use surface pressures between 0.5 and 2 bar at intervals of 500 mb
 224 with a variety of gas mixtures. All simulated atmospheres have 83-94% CO₂, 0-6% H₂, 1% CH₄,
 225 and any remainder to reach 100% is N₂ (with the exception of the simulations detailed below that
 226 use gas mixtures described in the literature). H₂O is treated as a trace gas in all simulations and
 227 is not assumed to ever make a substantive change to the mean molecular weight of the
 228 atmosphere. In most of our “dry” simulations, the atmosphere has no water vapor at the beginning
 229 of the simulation and there is a small amount of soil moisture. In a small subset of these
 230 simulations, there is a larger amount of initialized soil moisture.

231 We also conducted a series of simulations with gas mixtures and pressures described in
 232 the literature. Specifically, we simulate some of the gas mixtures and pressures of Wordsworth
 233 et al. (2017), Kamada et al. (2020), and Haberle et al. (2019). Wordsworth et al. (2017) used
 234 94% CO₂, 5% H₂, and 1% CH₄ with surface pressures of 1 or 2 bar. Kamada et al. (2020) used
 235 97% CO₂ and 3% H₂ (among others, but found some amount of seasonal melting began at that

236 point) and we simulated that gas mixture with surface pressures of 1, 1.5, and 2 bar. Haberle et
 237 al. (2019) used 90% CO₂ and 10% H₂ (again among others) and that was again simulated with
 238 surface pressures of 1, 1.5, and 2 bar.



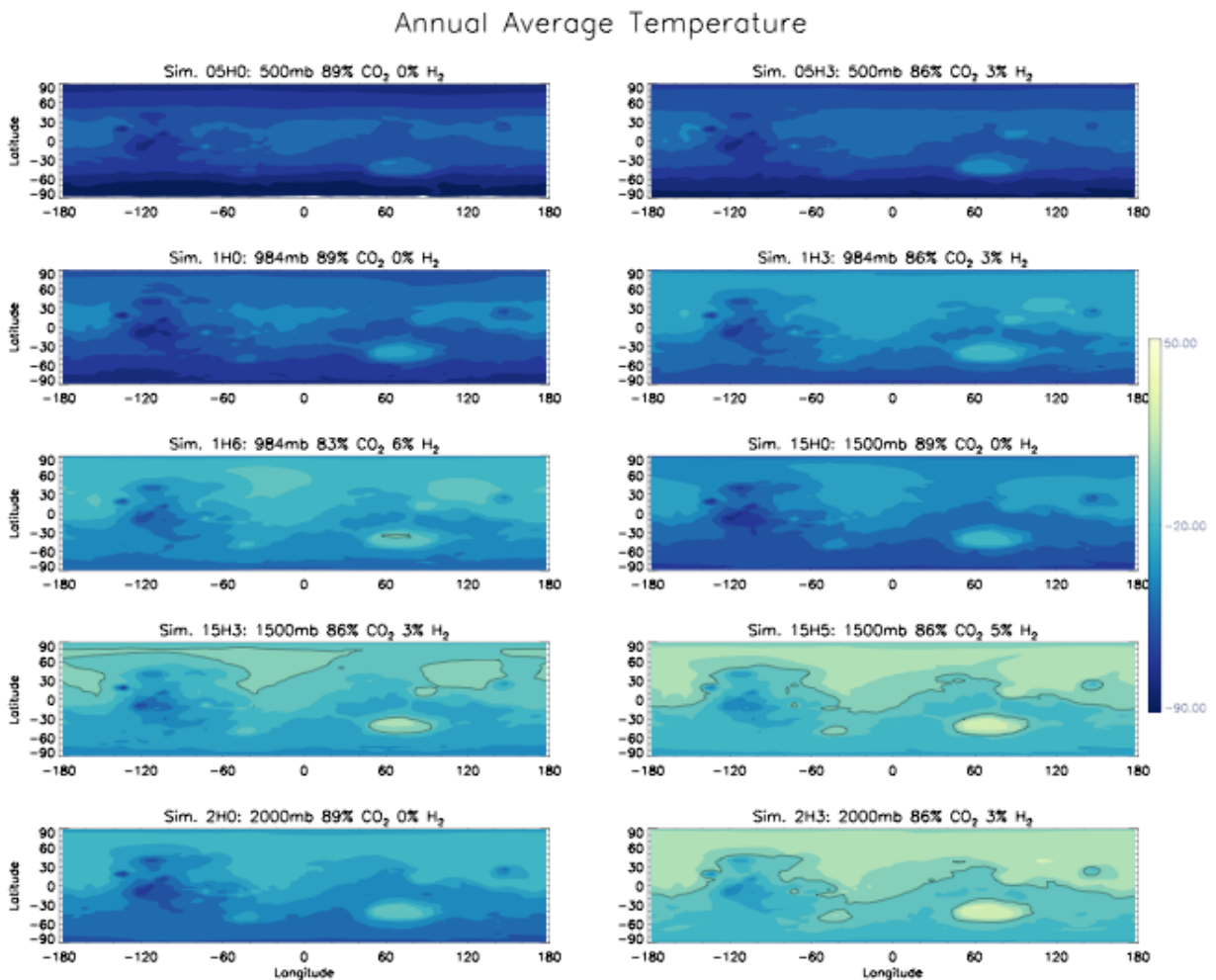
239
 240
 241 Figure 3: Global mean annual surface temperatures (°C) of “dry” ROCKE3D simulations as a
 242 function of surface pressure and H₂ abundance. Our gas mixtures are identified with circles,
 243 squares represent simulations using gas mixtures described by Haberle et al. (2019), stars
 244 represent simulations using Kamada et al. (2020) gas mixtures, and triangles represent
 245 Wordsworth et al. (2017) gas mixtures. Some simulations with similar surface pressures and H₂
 246 abundances are indicated with smaller symbols and slightly offset in pressure for clarity.
 247

248 Figure 3 shows global mean annual surface temperatures of 19 ROCKE3D simulations. A
 249 couple conclusions are immediately apparent from looking at Figure 3. First, without H₂ (and the
 250 associated CIA), even 2 bar pure CO₂ surface pressures are insufficient to produce global mean

251 annual surface temperatures above the freezing point of water. In fact, the 2 bar 0% H₂ simulation
252 (Simulation 2H0 from Table 1) has a global mean annual surface temperature of -29.1°C. This is
253 substantially warmer than a comparable atmosphere and pressure presented in Forget et al. (2013),
254 possibly due to the lack of CO₂ condensation in ROCKE-3D which would serve to warm the
255 middle atmosphere. Increasing H₂ abundance to 3-5% produces temperatures near freezing or
256 slightly above freezing for Simulations 2H3, RW2, and AK2. The other immediate conclusion
257 from Figure 3 is that 1 bar surface pressure is insufficient for global mean annual surface
258 temperatures above freezing, even with H₂ abundances of 10% as in Simulation RH1.

259 Compared to the published results that we have used as guidance for some gas mixtures
260 and pressures, we find generally good agreement. Wordsworth et al. (2017) used a line-by-line
261 spectral code to evaluate the climate impact of their *ab initio* calculations of CIA and found that
262 CO₂-H₂ mixtures reached 273 K with approximately 3% H₂ for 2 bar pressures and 5% H₂ at 1.5
263 bar pressures. Adding CH₄ reduced the amount of H₂ necessary for above freezing conditions. As
264 seen in Table 1, our simulations following Wordsworth et al. (2017) (RW simulations) all have
265 1% CH₄ and 5% H₂. The resulting global mean annual surface temperatures are quite comparable
266 to those shown by Wordsworth et al. (2017), with Simulation RW1 having a temperature of -
267 24.5°C, Simulation RW2 having a temperature of 14.0°C, and Simulation RW2wet (with higher
268 initial soil moisture) having a temperature of 15.7°C. The slightly warmer temperature for wetter
269 soil conditions is due to the higher water vapor amounts in the atmosphere. Haberle et al. (2019)
270 found that large impacts of iron-rich meteorites could degas substantial H₂ and that mixing ratios
271 of 10% or more produce temperatures above 273 K for 1 bar or thicker atmospheres. Our 1 bar
272 simulation, Simulation RH1 (90% CO₂ & 10% H₂), has a global mean annual surface temperature
273 of -13.5°C, but the simulations with thicker atmospheres, Simulations RH15 and RH2, have

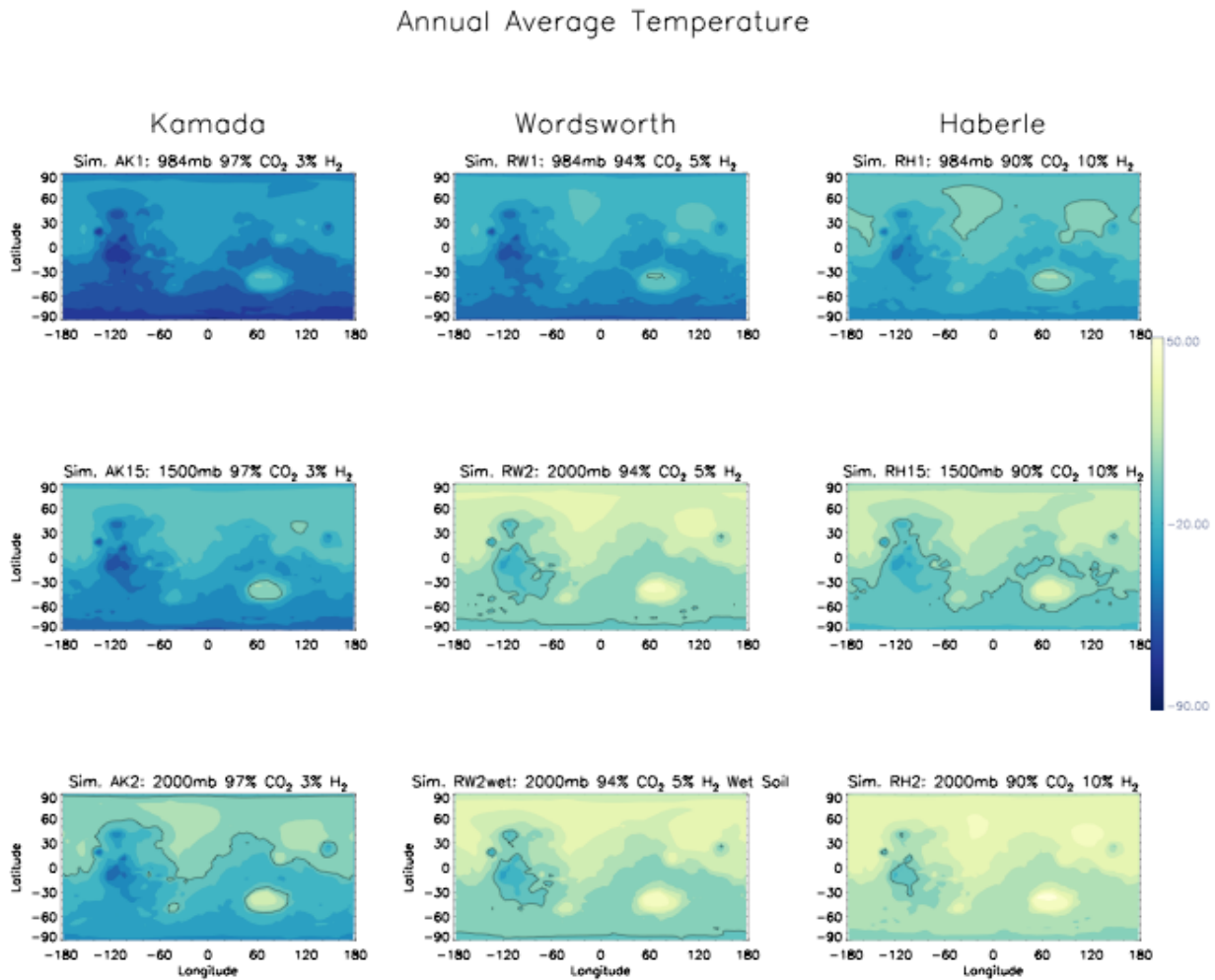
274 temperatures of 8.5°C and 23.9°C, respectively. Our simulations following Kamada et al. (2020)
275 are similar to their “Dry-Mars” simulations with 3% H₂ and result in temperatures quite similar to
276 theirs, with all three simulations (Simulations AK1, AK15, and AK2) having global mean annual
277 surface temperatures below freezing. Indeed, on balance, our simulation temperatures compare
278 quite favorably with the “Dry-Mars” simulations by Kamada et al. (2020), even for other mixing
279 ratios of H₂, and accounting for their higher (our lower) mixing ratios of CO₂ and our inclusion of
280 1% CH₄.



281

282

283 Figure 4. Mean annual surface temperatures ($^{\circ}\text{C}$) for 10 ROCKE-3D simulations with surface
 284 pressures and CO_2 and H_2 mixing ratios identified in the panel title. All simulations incorporate
 285 dry soil. The black line indicates the freezing point of water.



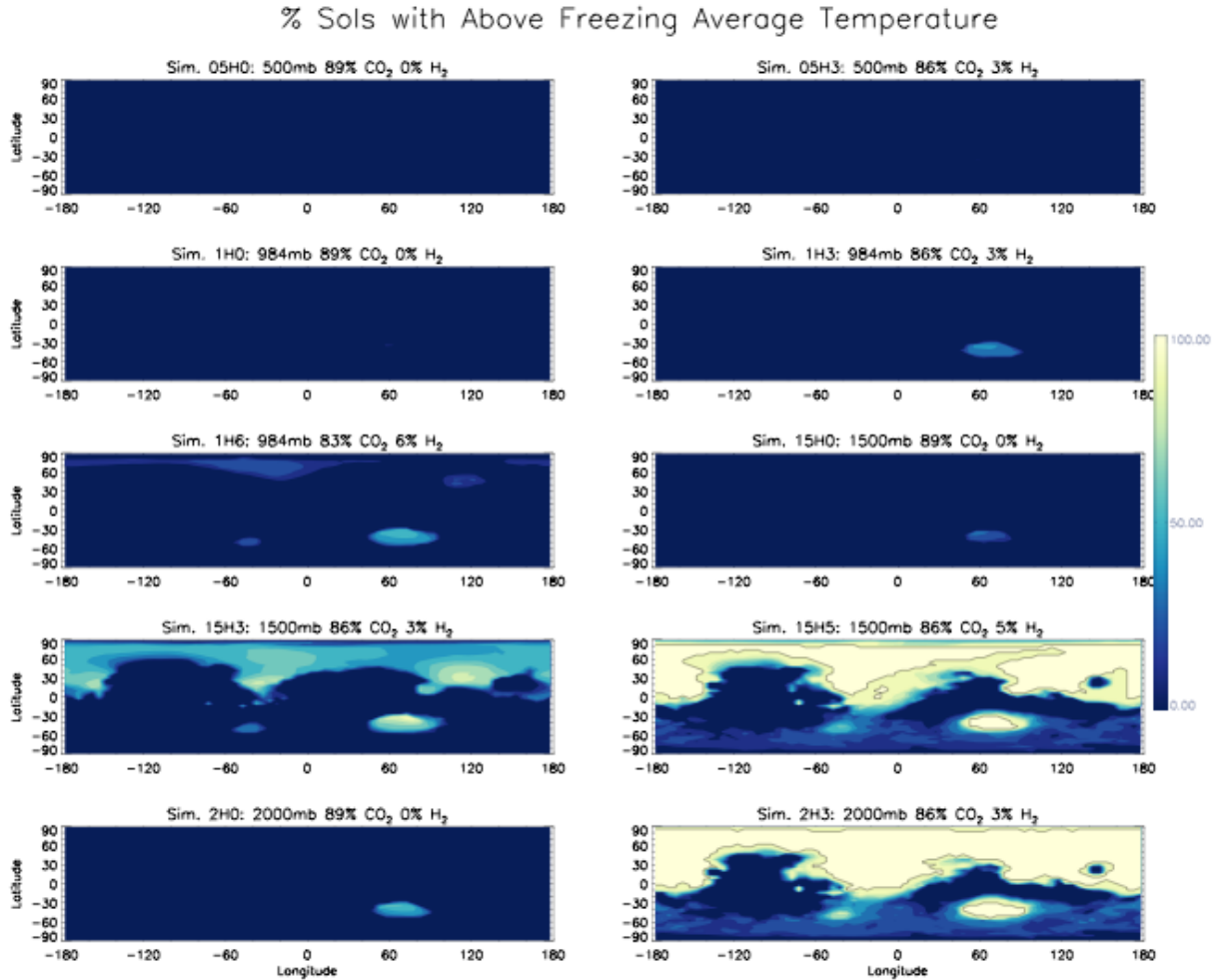
286
 287
 288
 289
 290
 291
 292

Figure 5. Same as in Figure 4, except for gas mixtures described in the literature as delineated above.

In Figures 4 and 5 we take a global view to see how temperatures vary. The same points discussed with Figure 3 generally continue to hold. Namely, even at 1 bar surface pressures, most or all of the planet sees annual average temperatures below freezing. With 5-6% H_2 , small regions of Hellas Basin see above freezing annual average temperatures and increasing that to 10% H_2 in Simulation RH1 expands that to portions of the northern hemisphere lowlands. Second, some

297 amount of H₂ is necessary to have any portion of the planet experience annual average
298 temperatures above the freezing point of water. Simulation 2H0 (bottom left panel of Figure 4)
299 shows no regions of the planet above freezing despite a 2 bar atmosphere of CO₂. All planets with
300 global mean annual average temperatures above -25°C have some region of the planet above
301 freezing on an annual average basis. Simulations with increasing surface pressure and H₂ amounts
302 eventually reach a point where most of the planet is above freezing (e.g., Simulation RH2) although
303 the high elevations of the Tharsis Montes and plateau remain below freezing in all simulations.
304 This is particularly relevant for cold-trapping of water, as will be discussed below.

305 Not surprisingly, but worth mentioning, is that the regions that preferentially experience
306 above freezing annual average temperatures are the topographic lowest spots in Hellas Basin and
307 the northern lowlands. The gradient in temperatures with topography is due to adiabatic effects
308 (Wordsworth et al., 2013), which modern Mars does not experience due to its thin atmosphere.
309 These are not the locations that have the highest density of valley networks and outflow channels,
310 which fall near the topographic dichotomy boundary and in the southern hemisphere highlands
311 (Hynek et al., 2010). This disparity is well-known from studies of possible ancient martian
312 climates (e.g., Palumbo and Head, 2018).



313

314

315 Figure 6. Percent of sols with above freezing daily average temperatures for 10 ROCKE-3D
 316 simulations with surface pressures and CO₂ and H₂ mixing ratios identified in the panel title. All
 317 simulations incorporate dry soil. The black line encloses the areas with 100%.

318

319 Looking at seasonal temperatures, we see in Figure 6 that 1 bar (with some H₂ present in

320 the atmosphere) or higher pressure simulations all experience some regions of the planet with daily

321 average temperatures above freezing, again predominantly in Hellas Basin or the northern

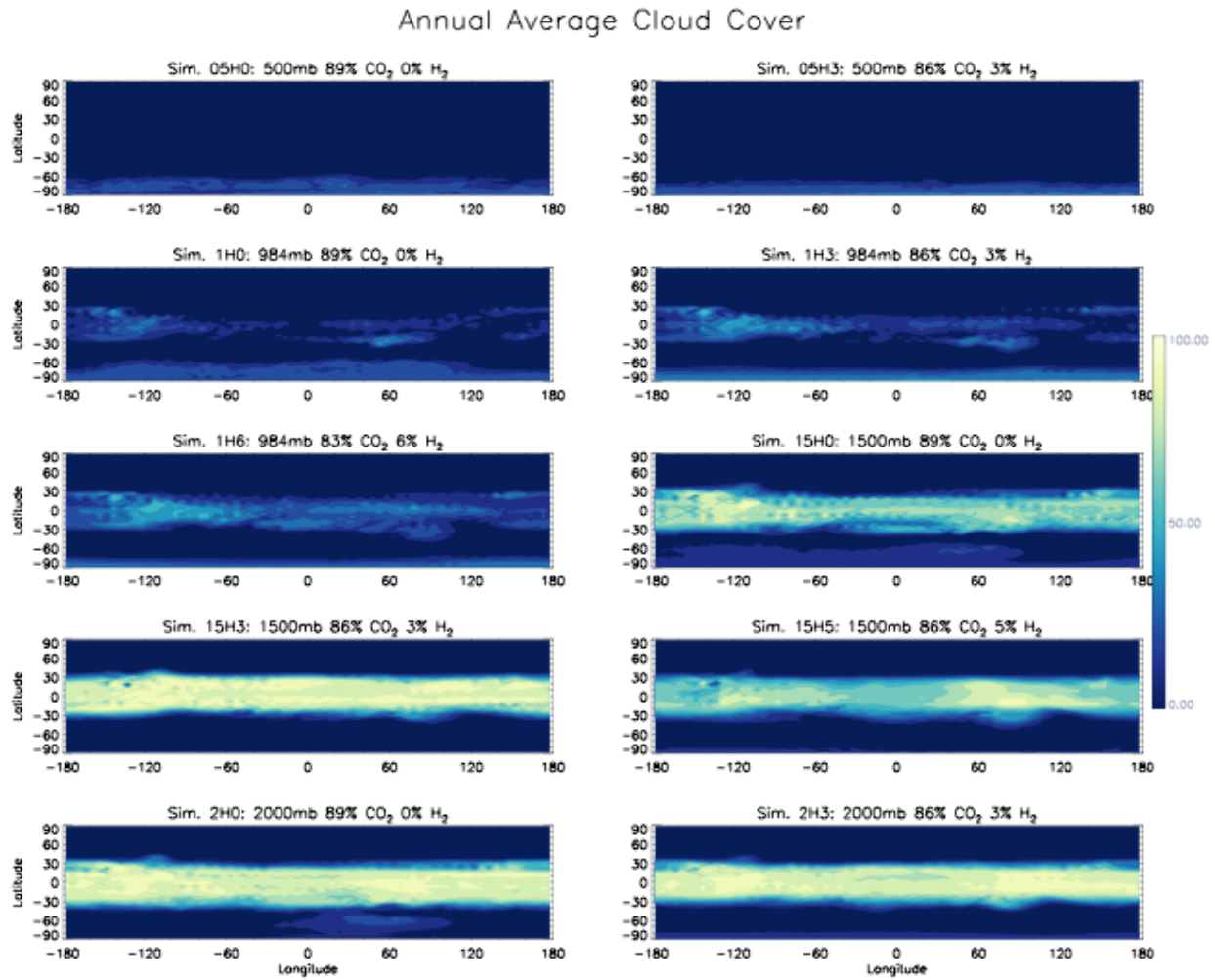
322 lowlands. In the highest pressure and H₂ mixing ratio, and thus warmest, simulations (bottom right

323 two panels of Figure 6) the northern lowlands and Hellas Basin are above freezing year-round.

324 Interestingly, however, even parts of the southern hemisphere highlands (e.g., Aonia Terra and

325 Terra Sirenum both south of the Tharsis plateau) experience seasonally warm temperatures and

326 some of those regions do exhibit high density of valley networks as shown by Hynek et al. (2010).
327 That is also true of areas near the topographic dichotomy boundary in the eastern hemisphere,
328 although the Terra Sabaea and Tyrrhena Terra regions (both with numerous valley networks) north
329 of Hellas remain below freezing all year.

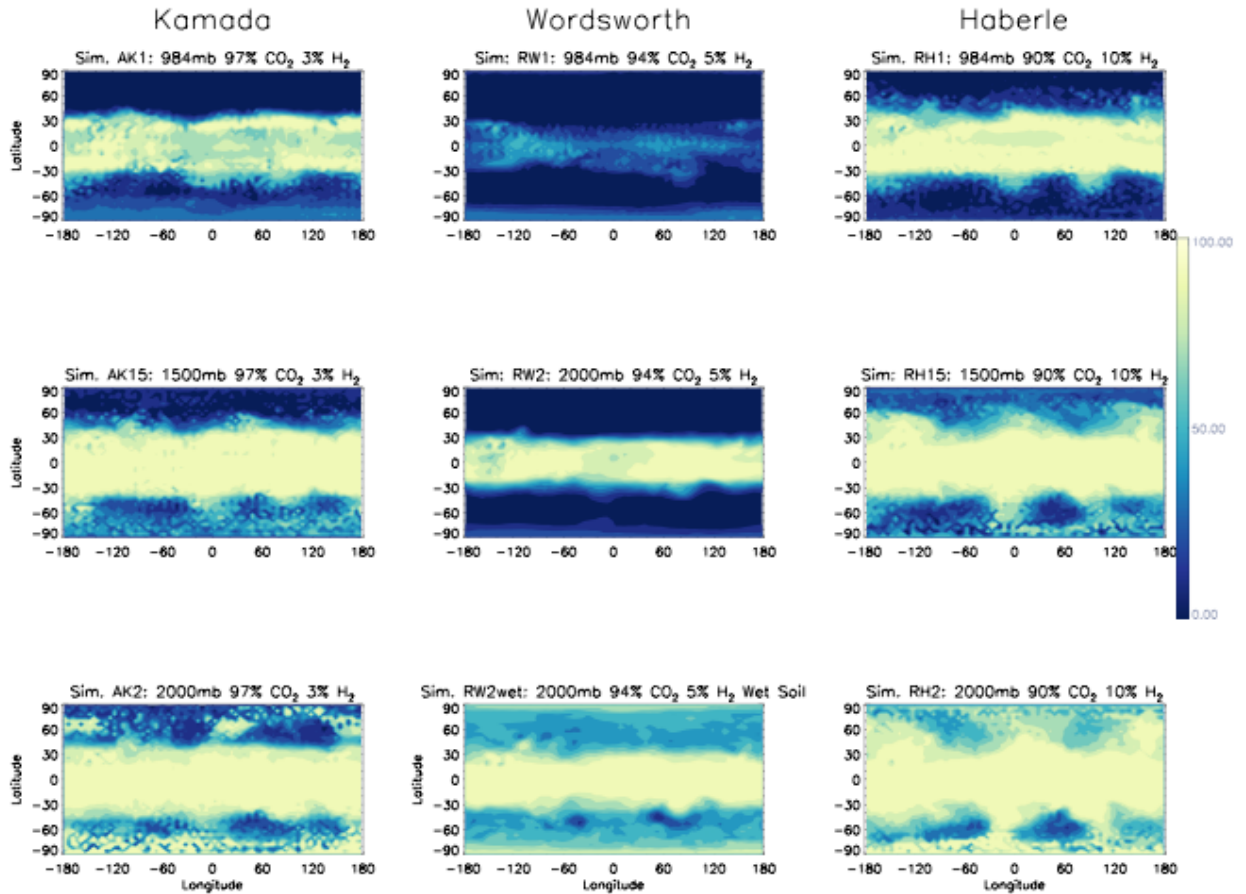


330
331
332 Figure 7. Annual average cloud cover for 10 ROCKE-3D simulations with surface pressures and
333 CO₂ and H₂ mixing ratios identified in the panel title. All simulations incorporate dry soil.
334
335 As stated above, our “dry” simulations (nearly) all use initial soil moisture conditions that
336 have a small amount of water present in the soil that is then moved through the climate system
337 following the water cycle parameterizations in the GCM. But despite the comparatively small

338 amount of water (relative to the simulations described below in Section 3.2) in the system, the
339 simulations do produce water cloud cover. Even for modern terrestrial climate studies,
340 understanding the complete climatic influence of clouds remains an area of ongoing research and
341 much work has been done about how clouds (both H₂O and CO₂) may have impacted the ancient
342 climate of Mars (e.g., Forget et al., 2013).

343 Figure 7 shows that substantial clouds are found in the tropics. Although some convective-
344 type clouds occur over Tharsis, the bulk of the clouds are thin cirrus-like water ice clouds. The
345 coldest simulations (low pressure and lower H₂ mixing ratios) have generally clear atmospheres,
346 with infrequent tropical clouds as well as seasonal clouds over the south pole. Warmer simulations
347 (high pressure and higher H₂ mixing ratios) have a well-defined tropical cloud belt between 30°S
348 and 30°N with little longitudinal variation. Some simulations (e.g., Simulation 2H0, bottom left
349 panel of Figure 7) additionally suggest that Hellas basin sees some amount of cloud cover, which
350 is true even in the modern climate.

Annual Average Cloud Cover



351

352

353 Figure 8. Same as in Figure 7, except for gas mixtures described in the literature as delineated
354 above.

355

356 The depiction of clouds in the dry simulations is more complicated than seen in Figure 7,

357 however, as shown in Figure 8. Whereas the 1 bar simulations in Figure 7 all have generally clear

358 atmospheres, Figure 8 shows that Simulations AK1 and RH1 are much cloudier, more so even than

359 the 2 bar simulations in Figure 8. In all cases (Figures 7 and 8), the clouds depicted are thin cirrus-

360 like water ice clouds and have peak ice mixing ratios in the 100-200 mb pressure levels (see also

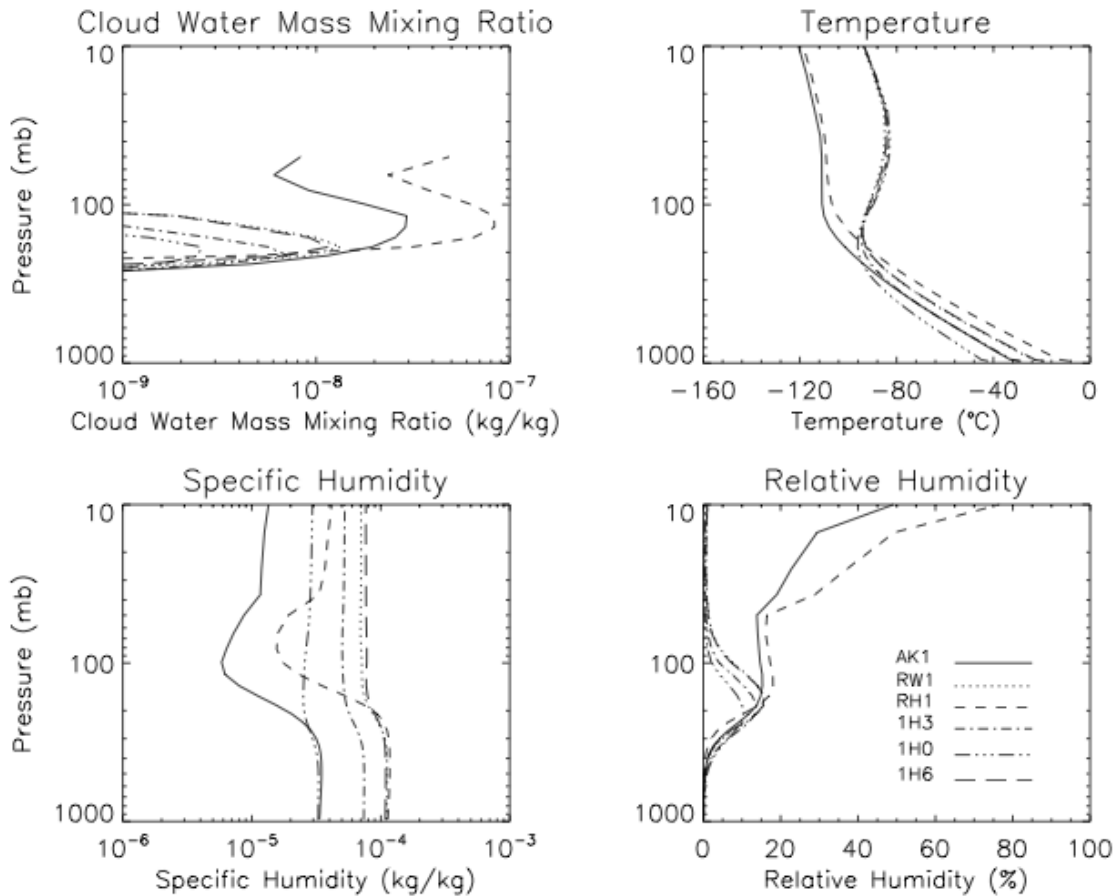
361 Figure 9). Despite their broad coverage, they have minimal net radiative effect ($\sim O(1)$ W/m²).

362 That pattern of the Kamada and Haberle simulations being both much cloudier than the
363 Wordsworth simulations and those in Figure 7, even when adding in a wetter soil moisture initial
364 condition (Simulation RW2wet, bottom center panel of Figure 8), continues at higher pressures as
365 well. The reason is ultimately their disparate atmospheric gas compositions. All simulations in
366 Figure 7 and the Wordsworth simulations in Figure 8 all include 1% CH₄. As shown by Bryne
367 and Goldblatt (2015) for the Archean Earth, 0.1% CH₄ and higher mixing ratios facilitate strong
368 shortwave absorption in the troposphere and stratosphere. Wordsworth et al. (2017) also saw this
369 higher altitude warming from CH₄. This stronger shortwave absorption is reflected in the most
370 recent updates of the HITRAN database that ROCKE-3D uses (e.g., Rothman et al., 2013; Brown
371 et al., 2013), but was not reflected in earlier versions. Higher CH₄ mixing ratios produce sufficient
372 absorption to create a distinct tropopause, and this is precisely what we see when looking at our
373 simulations (Figure 9). Despite higher specific humidities in the Wordsworth simulations and
374 those in Figure 7, the warmer upper troposphere temperature and reduced tropospheric relative
375 humidity limits the cloud production (see Figure 9), relative to the Kamada (AK1) and Haberle
376 (RH1) simulations without CH₄. Increased static stability limiting cloud production in our
377 simulations with CH₄ is analogous to similar studies of Archean Earth that removed O₂ and O₃ and
378 noted this resulted in decreased cloud production (e.g., Wolf and Toon, 2013).

379 From the perspective of these simulations, the difference in cloud cover is ultimately due
380 to warmer upper tropospheric temperatures. In all variables relevant to cloud production, the
381 simulations without CH₄ are distinct from simulations with it (Figure 9). Simulations AK1 and
382 RH1, without CH₄, exhibit cooler upper tropospheric temperatures and produce both thicker and
383 more widespread cloud cover. Despite the simulations with CH₄ having a distinct tropopause, the
384 temperature inversion is weak and water is not substantially cold-trapped. Indeed, specific

385 humidity values only slightly reflect the temperature inversion in the simulations with CH₄ (Figure
 386 9). This “leaky” tropopause is similar to that on Titan, where CH₄ still mixes into the stratosphere
 387 and mesosphere and is eventually photodissociated and destroyed (e.g., Roe, 2012). Indeed, a
 388 hygropause is more efficiently produced by the thick cloud cover preventing vertical water
 389 transport (see Simulation AK1 in Figure 9). Water ice clouds also limit vertical water transport in
 390 the modern martian climate system (Clancy et al., 1996; Navarro et al., 2014). This result suggests
 391 that comparatively subtle features such as trace gas mixing ratios (i.e., CH₄ in this case) and cloud
 392 cover may have been important for water loss in the early martian climate system.

393



394

395 Figure 9. Average vertical profiles of cloud mass mixing ratio, temperature, specific humidity,
396 and relative humidity for the 30°S-30°N latitude band for 6 ROCKE-3D simulations (as identified
397 in the relative humidity panel).

398

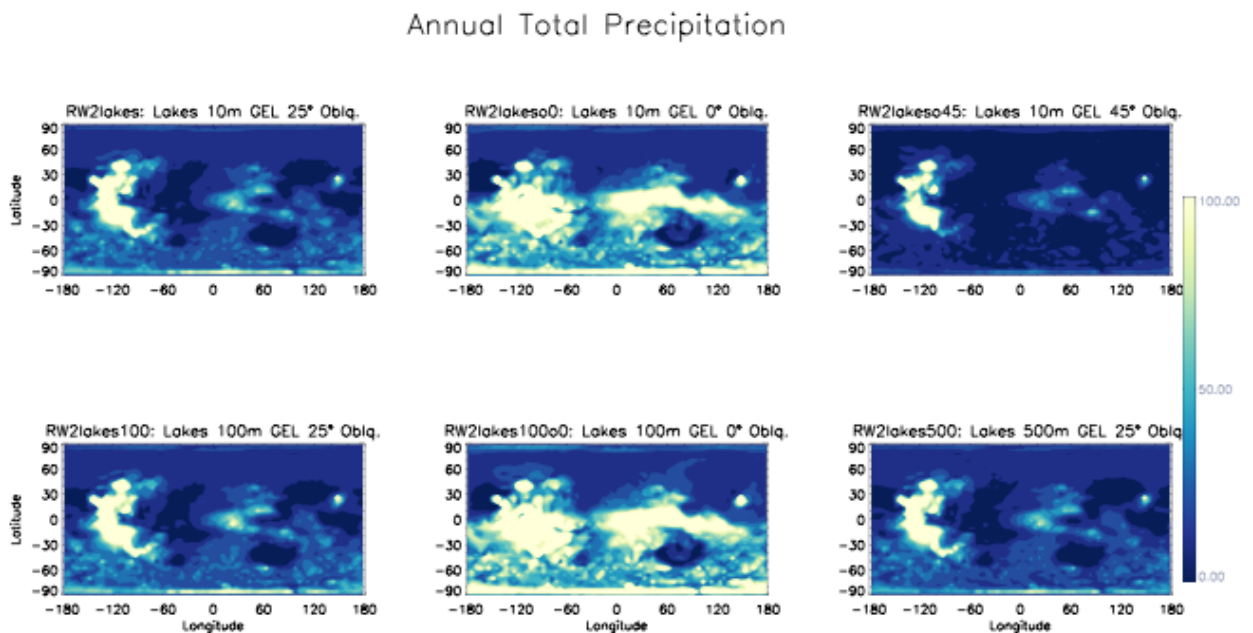
399 3.1. Wet Simulations

400 Our next set of simulations are initialized with surface liquid water in the form of active
401 lakes. Those lakes are then depleted or replenished based on the precipitation and evaporation
402 patterns within the simulation. The first set of these “wet” simulations uses the RW2 simulation
403 gas mixture (94% CO₂, 5% H₂ & 1% CH₄) and modern topography. Each simulation is run until
404 hydrologic equilibrium is reached, which always takes much longer than radiative equilibrium.
405 We define hydrologic equilibrium as the point where hydrologic variables (e.g., mass of water in
406 lakes, mass of ground water, mass of ground ice, snow depth, and ocean ice fraction) are in steady-
407 state.

408 Using modern topography, hydrologic equilibrium is always reached with all lakes on the
409 planet being completely depleted and the remaining water in the climate system consisting of
410 surface and subsurface snow and ice and ground water. This is due to the cold trapping of nearly
411 all the planet’s water on Tharsis, and to a lesser degree, the south pole. Wordsworth et al. [2015]
412 also describe this cold-trapping at Tharsis and the poles with modern topography (see also
413 Palumbo and Head [2018]). The annual precipitation patterns for this first set of six simulations
414 is shown in Figure 10. The heaviest precipitation consistently falls on the upwind (westward) side
415 of Tharsis, particularly Arsia Mons, for every simulation except those with 0° obliquity. In fact,
416 the maximum annual precipitation (707 mm) occurs in the RW2lakes simulation (upper left panel
417 of Figure 10), with only 10 m of GEL water.

418 In simulations with modern obliquity or 45° obliquity, there is a prominent rain shadow
419 east of Tharsis (see also Wordsworth et al. (2015)). Comparing with Figure 11, which only shows
420 liquid precipitation, indicates that much of the precipitation that falls over Tharsis and the south

421 pole falls as snow. However, the simulations with 0° obliquity are distinctly different (middle two
422 panels of Figure 10 and 11). Simulations with 0° obliquity show much more widespread
423 precipitation, with precipitation on both sides of Tharsis, across the topographic dichotomy
424 boundary and through the southern highlands. Maximum precipitation at a given location (also in
425 Tharsis) is somewhat less, however, at ~ 500 mm per year. Notably, the simulations with
426 0° obliquity have much more *liquid* precipitation than those with 25° or 45° and it is fairly evenly
427 distributed across the low and middle latitudes including across locations with valley network
428 formations [Hynek et al., 2010].

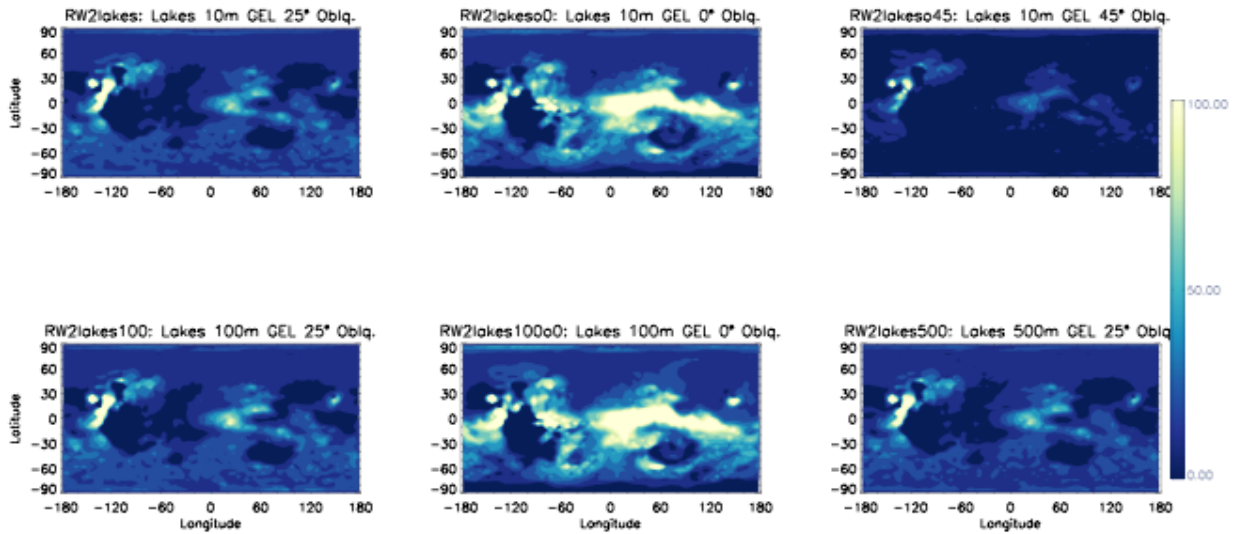


429

430

431 Figure 10. Annual total precipitation (mm) for 6 ROCKE-3D simulations distinguished by total
432 initial water inventory and obliquity. All water is initialized in lakes and then moved through the
433 climate system.

Annual Total Liquid Precipitation



434
435

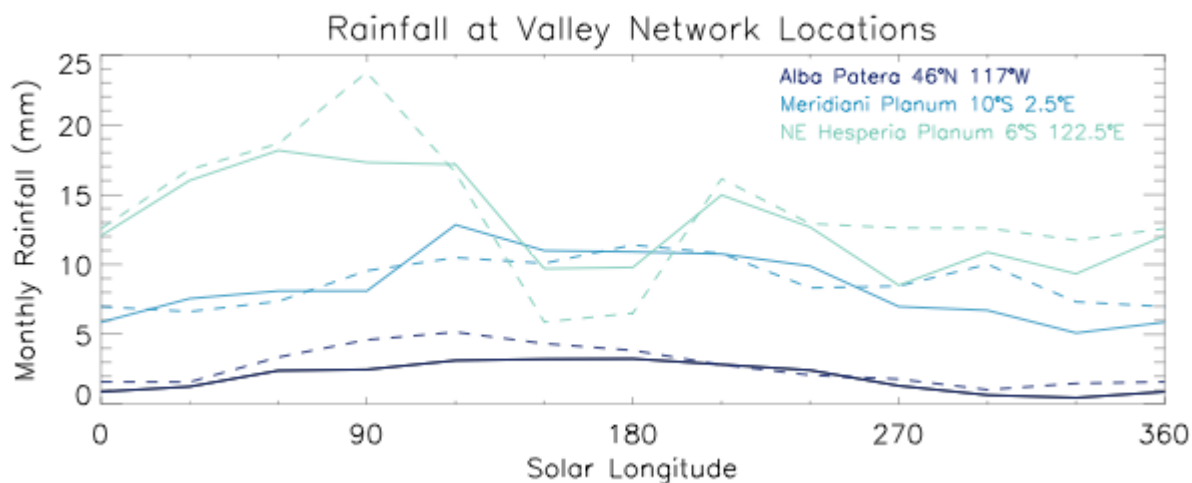
436 Figure 11. Same as Figure 10 except for annual total liquid precipitation (mm).
437

438 Simulations with modern or 45° obliquity show little precipitation in areas with valley
439 network formations, regardless of the planet's initial water inventory. In fact, simulations with
440 45° obliquity (often suggested to be a “warmer” climate state in the literature [Palumbo and Head,
441 2018]) is the driest simulation over the southern highlands where valley networks are seen. Again
442 there is minimal change to precipitation in the 0° obliquity simulations based on initial water
443 inventory, but there is a slight increase with 100m GEL (bottom middle panel of Figures 10 and
444 11) relative to the 10m GEL simulation (top middle panel of Figures 10 and 11).

445 0° obliquity during martian history has not been thoroughly explored in the literature,
446 particularly using three-dimensional GCMs. This is perhaps due to the expected collapse of a
447 CO₂-dominated atmosphere into polar ice caps. Note, this version of ROCKE-3D does not have
448 CO₂ condensation physics, as mentioned above, but mean annual temperatures in this simulation
449 are well above the CO₂ frost point at all locations on the surface and the obliquity drives minimal
450 seasonal variation. Our simulations show that 0° obliquity is the most plausible for producing

451 rainfall and associated runoff and erosion capable of creating the valley network formations. We
 452 show this in more detail in Figure 12. We plot “monthly” (approximately 30° of solar longitude)
 453 rainfall using three sample areas from Hynek et al. [2010] that have high drainage density across
 454 the planet. All three locations show modest rainfall throughout the martian year. As stated above,
 455 increasing the initial water inventory of the planet does not substantially alter the final hydrological
 456 balance when the simulations use modern topography. Note however, that there is not perfect
 457 congruence between valley network formation locations and predicted rainfall in our simulations
 458 with 0° obliquity. For example, locations south of Tharsis such as the highlands of Solis Planum,
 459 see near-zero rainfall in our simulations. Those locations such as Solis Planum do see snowfall
 460 however, and annual average temperature there is near freezing so some seasonal melting is
 461 plausible. Episodic snowmelt and runoff is another plausible formation mechanism for some
 462 valley network formations (e.g., Wordsworth et al., 2015; Palumbo et al., 2020).

463



464

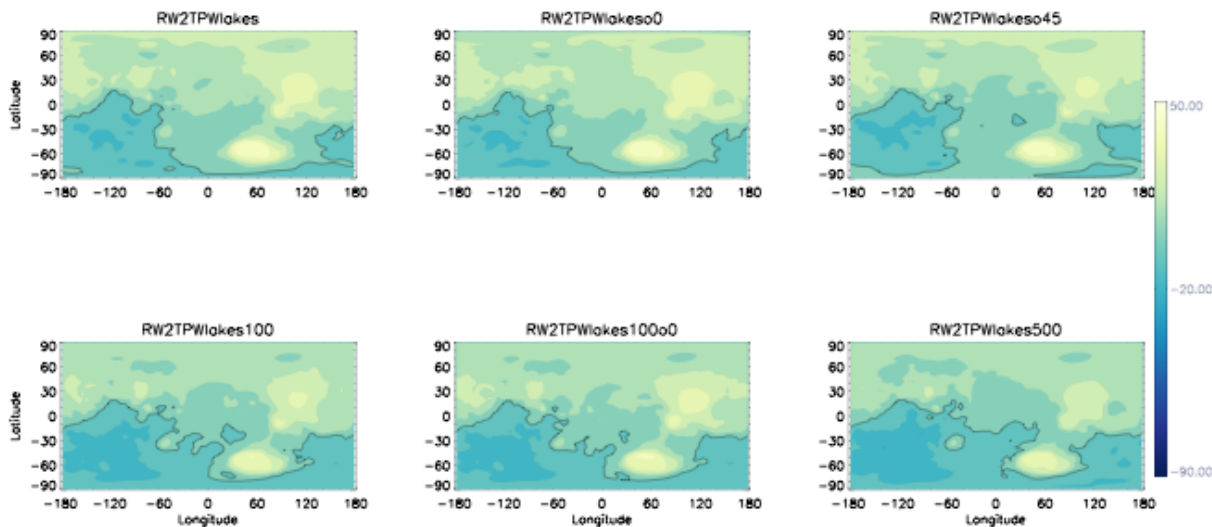
465 Figure 12. Simulated annual rainfall at three locations with high drainage density per Hynek et
 466 al. [2010]. Solid lines indicate simulation RW2lakeso0 with 10m GEL initial water inventory and
 467 dashed line indicates simulation RW2lakes100o0 with 100m GEL initial water inventory.
 468 Locations are specified in the figure.

469

470

471 Our second set of “wet” simulations also uses the RW2 simulation gas mixture, but uses a
472 plausible topographic map before the formation of Tharsis and associated true polar wander. We
473 use the map from Bouley et al. (2016) (see also Matsuyama and Manga, 2010). The timing of the
474 formation of Tharsis relative to the formation of the valley networks and lake systems on Mars is
475 critical for understanding the plausible climate of the late Noachian. The lack of Tharsis to serve
476 as a strong cold trap produces a much more robust hydrological cycle. Using the paleotopography,
477 annual mean surface temperatures are comparable or slightly cooler (1-2 K) than the same
478 simulation using modern topography (Figure 13). However, the coldest mean annual surface
479 temperatures on the planet are ~10 K warmer in the paleotopography simulations. This is sufficient
480 to prevent the extreme cold trapping of water that is seen on the Tharsis plateau when using modern
481 topography. Additionally, because water is not as extensively cold trapped and more is actively
482 circulating hydrologically, the global mean surface temperature is slightly dependent on the initial
483 water inventory. Simulations initialized with 100 m or 500 m GEL water inventories are 5-9 K
484 colder than equivalent simulations with 10 m GEL initial water inventory. This is due to increased
485 snow and ice coverage and more widespread clouds in simulations with greater water inventories.
486 Notably, the simulations with 0° obliquity are again the warmest. For example, the three
487 simulations with 10 m GEL water inventory and obliquities of 0°, 25.19°, and 45° have global
488 annual mean surface temperatures of: 13°C, 11.8°C, and 9.9°C, respectively.

Paleo Topography Annual Average Temperature



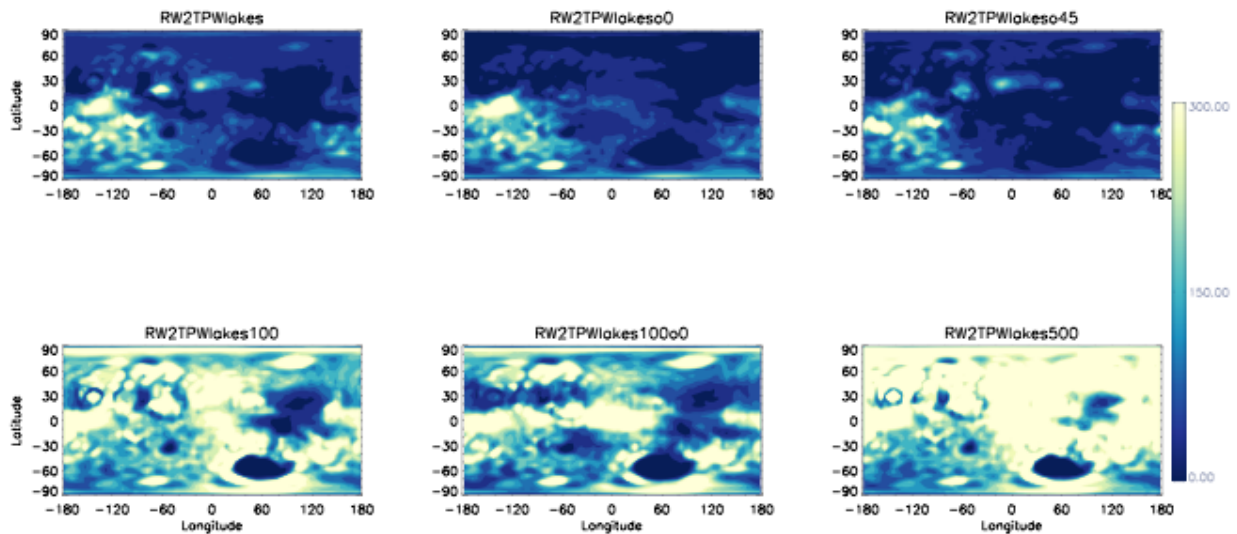
489
490 Figure 13. Mean annual surface temperatures ($^{\circ}\text{C}$) for 6 ROCKE-3D simulations using the
491 martian paleotopography of Bouley et al. [2016] and distinguished by total initial water inventory
492 and obliquity. The black line indicates the freezing point of water. See Table 1 for descriptions of
493 each simulation.

494
495 Assuming the valley networks formed prior to Tharsis formation and associated true polar
496 wander, they would be placed in an east-west oriented band centered in the southern low latitudes
497 near 24°S [Bouley et al., 2016]. By eye it can be seen from Figure 13 that the western portion of
498 this band is higher (and hence colder) terrain while the center and eastern band is lower (and hence
499 warmer) terrain. Figures 14 and 15 display annual total precipitation and annual total liquid
500 precipitation for six simulations using the paleotopography and can be directly compared with
501 Figures 10 and 11, which used the modern topography. However, note that the scales of those two
502 sets of figures are different to better highlight areas of higher precipitation in the paleotopography
503 simulations.

504 Simply, there is far more precipitation in simulations with paleotopography. Each
505 simulation with paleotopography has higher maximum precipitation than the comparable
506 simulation with modern topography. However, as can be seen by comparing Figures 14 and 15,
507 those maxima occur as snowfall over the high terrain in the southwest hemisphere of the planet.
508 Unlike the simulations with modern topography, precipitation increases with increasing global
509 water inventory. Simulations with 100 m or 500 m GEL water inventories see far more
510 precipitation in the northern hemisphere due to the more abundant surface liquid water (in the form
511 of lakes) in the northern hemisphere lowlands in those simulations.

512

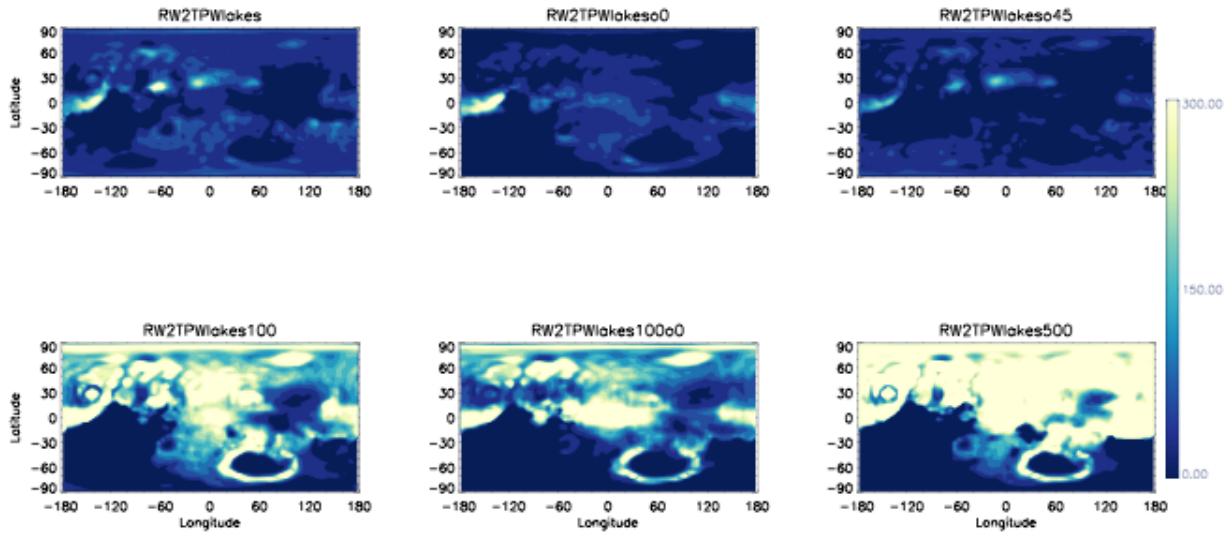
Paleo Topography Annual Total Precipitation



513

514 Figure 14. Annual total precipitation (mm) for 6 ROCKE-3D simulations distinguished by total
515 initial water inventory and obliquity and using martian paleotopography. All water is initialized in
516 lakes and then moved through the climate system. Note the different scale relative to Figure 10.
517 See Table 1 for descriptions of each simulation.
518

Paleo Topography Annual Total Liquid Precipitation



519

520 Figure 15. Same as Figure 14 except for annual total liquid precipitation (mm).

521

522

523 Figure 15 shows that the planet is strongly divided between locations with predominant
524 snowfall and those with predominant rainfall in the paleotopography simulations. Comparing
525 Figure 15 to Figure 13 shows that areas with annual mean temperatures below freezing see very
526 little or no rainfall. Much of the rainfall occurs in the northern hemisphere in all the simulations,
527 but there is rainfall in the southern hemisphere low latitudes, particularly from 60°W to 180°E.
528 This partially overlaps the expected region of the valley network formations if they formed prior
529 to Tharsis and associated true polar wander [Bouley et al., 2016], but the western portion of this
530 region does not have any significant rainfall in any of our simulations. Using the paleotopography,
531 the simulations with either 0° or modern (25.19°) obliquity produce rainfall in this latitude band,
532 with slightly more rainfall in the simulations with modern obliquity. Again, 45° obliquity is not
533 consistent with rainfall over locations with valley network formations.

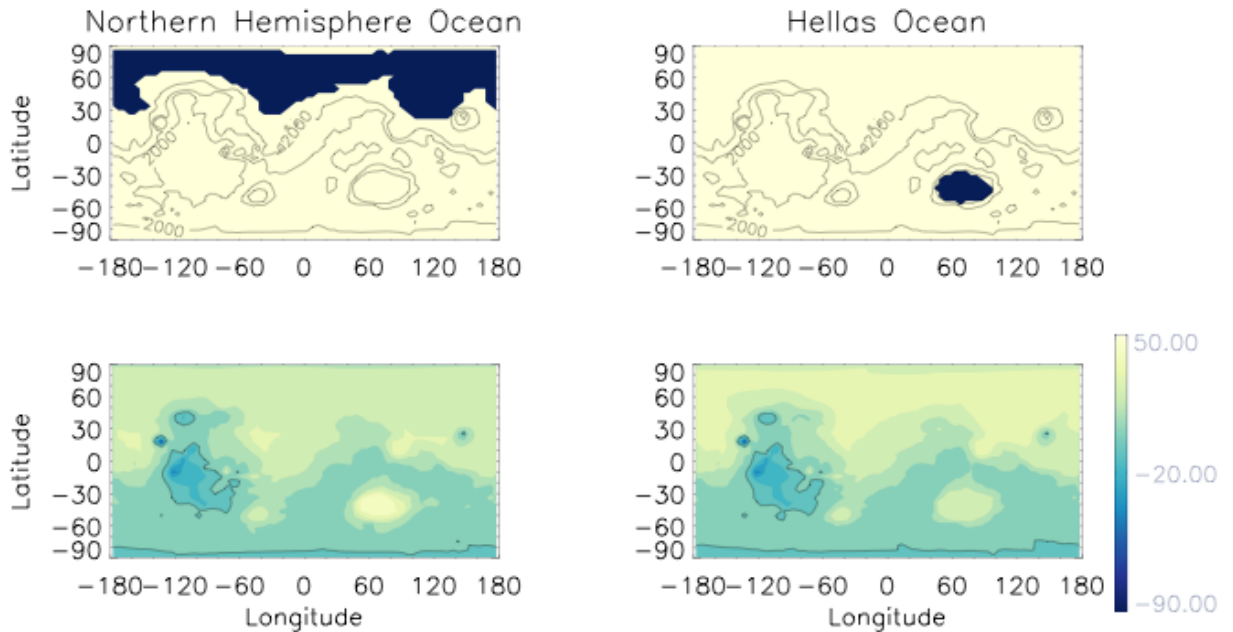
533

3.2. Ocean Simulations

534 Our final set of simulations uses ROCKE-3D's fully coupled dynamic ocean capability.
535 Most other published ancient Mars ocean simulations used mixed layer oceans (e.g., Kamada et
536 al. (2020)). All previously discussed simulations with surface liquid water use dynamic lakes that
537 form or evaporate based on precipitation patterns. In these simulations, water is initialized in
538 oceans. We began a wide spectrum of such simulations, but the majority did not reach radiative
539 and hydrological equilibrium before a shallow point of the ocean froze across the full depth. This
540 freezing crashes the model and ends the simulation. Two ocean simulations did reach equilibrium,
541 all using modern topography and obliquity values. Following a long history of research discussing
542 the possibility of an ancient martian northern hemisphere ocean (e.g., Di Achille and Hynek, 2010),
543 we simulate such a northern ocean. Additionally, since Hellas basin is the lowest topographic
544 point on the planet, we conduct a simulation with a Hellas ocean. Here we introduce the impacts
545 of these oceans on the broader planetary climate and reserve more in-depth analysis (hopefully
546 with additional successful simulations) to future work.

547 Figure 16 provides an initial orientation to our two simulations with fully coupled dynamic
548 oceans. The northern hemisphere ocean fills the northern lowlands Arcadia, Acidalia, and Utopia
549 Planitae to the -3900 m isohypse, whereas the Hellas ocean fills much of that basin to the same
550 level. The bottom two panels of Figure 16 should look quite similar to those of the bottom middle
551 two panels of Figure 5 since they use the same atmospheric gas composition. The subtle
552 differences relate to the moderating influence of the oceans. The ocean basins are cooler than
553 equivalent land surfaces in comparable simulations.

554



555

556 Figure 16. The location of the northern hemisphere ocean and Hellas ocean (dark fill) and
 557 planetary topography (lines contoured at -2000, 0, and 2000 m; top row). The annual average
 558 surface temperatures for those two simulations ($^{\circ}\text{C}$; bottom row).
 559

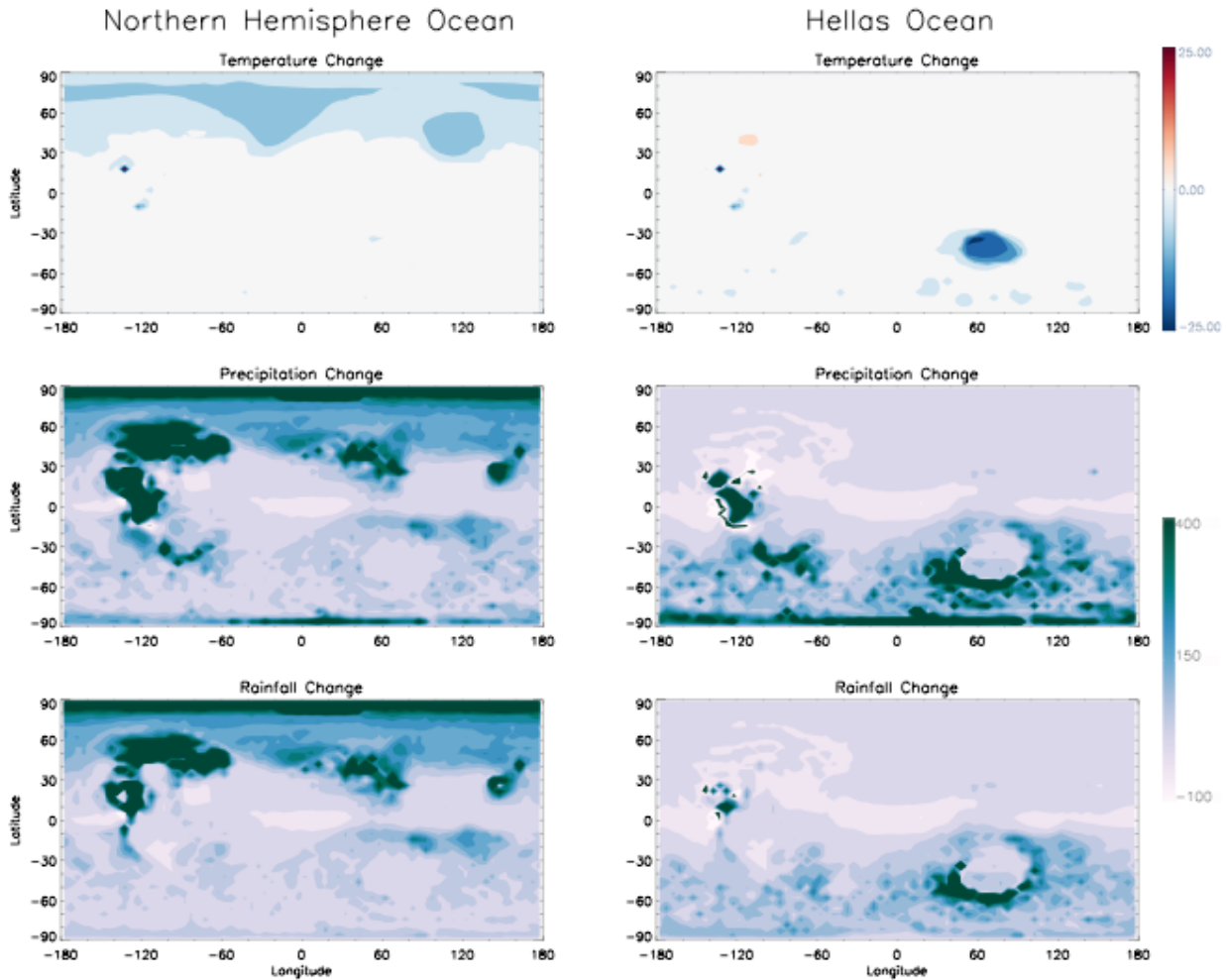
560 Our goal for the ocean simulations was to see if the abilities of oceans to alter planetary
 561 climates through ocean heat transport, their great thermal inertia, and changing atmospheric flows
 562 and precipitation patterns could be manifested in a way that would make a temperate Noachian
 563 climate on Mars more durable. In other words, would the creation of a Noachian ocean on Mars
 564 help stabilize and warm the climate in a way that would help perpetuate that temperature climate
 565 for a longer duration than might otherwise be true? To diagnose this, we compare our two ocean
 566 simulations with the RW2lakes simulation. The ocean simulations have identical atmospheric
 567 pressure and gas compositions to the RW2lakes simulation as well as using modern topography
 568 and obliquity. As noted earlier, when using modern topography, the initial water inventory of the
 569 planet did not alter the final stable end climactic state, so no significant difference would be found
 570 in comparing the ocean simulations to the RW2lakes500 (with 500 m GEL water), for example.

571 Figure 17 demonstrates how the two ocean configurations alter the simulated climate. As
572 seen in the top row, there is very little difference ($<1^{\circ}\text{C}$) in annual average surface temperature for
573 most of the planet if an ocean is present. Only the ocean itself, which is notably cooler than open
574 dry ground, produces a change to annual average temperatures. This alone answers one of our
575 questions regarding the influence of an ancient ocean on Noachian martian climate. Both a
576 northern hemisphere or Hellas ocean are inefficiently distributed to allow substantial meridional
577 heat transport which could help warm the planet and redistribute energy through the climate
578 system. Hence, there is a marginal effect on planetary surface temperature. Note however, that a
579 2 bar martian atmosphere does have very efficient *atmospheric* meridional heat transport due to
580 the greater mass per unit area relative to Earth. The effect of atmospheric density on heat transport
581 is discussed in the context of tidally-locked planets around M-stars by, e.g., Joshi et al. (1997) and
582 Wordsworth (2015).

583 There is however a notable change in precipitation patterns around the planet. This is
584 expected due to the larger surface liquid water inventory allowing increased evaporation and more
585 available liquid water in the climate system. Recall that one key finding of the simulations with
586 surface liquid water initialized in active lakes is that water is cold-trapped on Tharsis. The ocean
587 simulations do produce widespread snow and ice cover on Tharsis, as did those with active lakes,
588 but the simulation can not evaporate the ocean and redeposit it as snow on Tharsis as may happen
589 over geologic time in such a situation. These ocean simulations are hydrologically equilibrated,
590 but it is reasonable to assume that ocean depth would drop slowly through time as water is
591 deposited at the south pole and Tharsis. Indeed, as shown in Figure 17, precipitation near Tharsis
592 is increased in these simulations, particularly for the northern hemisphere ocean simulation (to be
593 expected given the proximity of the ocean to the Tharsis highlands). The Hellas ocean sees

594 increased precipitation throughout the southern hemisphere, while the greatest change for the
595 northern hemisphere ocean simulation is over that ocean itself.

596 Most notably, rainfall increases throughout the southern hemisphere and along the
597 dichotomy boundary, including over many locations with valley network formations, with the
598 Hellas ocean simulation. In the northern hemisphere ocean simulation, there is also a modest
599 increase of rainfall along the dichotomy boundary (particularly from 60-150°E). There is also
600 much more rainfall near Elysium Mons (25°N, 140°W).



601
602 Figure 17. Change in annual average surface temperature (°C, top row), change in annual
603 precipitation (mm, middle row), and change in annual rainfall (mm, bottom row) when comparing
604 the RW2lakes simulation to the northern hemisphere ocean simulation (left column) and Hellas
605 ocean simulation (right column).
606

607 4. CONCLUSIONS

608

609 In this work we sought to test whether the climate on Noachian Mars could have maintained
610 “warm and wet” conditions with reasonable constraints on surface air pressure (2 bar or less) and
611 the possible availability of H₂-CO₂ collision-induced absorption using ROCKE-3D, a capable and
612 flexible GCM. With ROCKE-3D, the answer to this question is “yes.” CO₂-dominated
613 atmospheres with surface pressures above ~1.5 bar and H₂ mixing ratios of ≥3% produce
614 global mean surface temperatures above the freezing point of water.
615 Our work is agnostic to the source of the H₂ and its duration in the atmosphere.

616 Note however, that in these initial simulations without significant amounts of water
617 (indeed, with a global water inventory more akin to modern Mars), the warmest locations are in
618 the northern hemisphere lowlands and Hellas basins. These are both locations far removed from
619 the places with geologic evidence of past fluvial activity in the southern hemisphere highlands
620 near the topographic dichotomy boundary and elsewhere. Much of the southern hemisphere and
621 Tharsis region have annual average temperatures well below freezing.

622 Additionally, some of our tested atmospheric gas mixtures included CH₄. We found that a
623 small amount of CH₄, 1% in our simulations, could have had important implications for ancient
624 water loss on Mars. Simulations that included CH₄ produce a weak and leaky stratosphere, where
625 warming temperatures limit water cloud formation, but where the upper tropospheric cold trap is
626 insufficient to limit vertical transport of water into the stratosphere where it could be
627 photodissociated and lost to space. Simulations without CH₄ have thicker water clouds in the
628 upper troposphere that acts as a more efficient hygropause, reducing water flux into the upper
629 atmosphere. Future work should address the implications of CH₄ and water ice clouds on water
630 loss from Noachian Mars in more detail.

631 After finding an atmospheric gas mixture that produced global mean temperatures above
632 freezing (RW2 = 94% CO₂, 5% H₂, and 1% CH₄ following Wordsworth et al. [2017]), our second
633 set of simulations looked at the hydrological cycle of the planet under these possible warm and
634 wet conditions. Using modern topography, the vast majority of water on the planet, regardless of
635 the initial water inventory, is cold-trapped on the high and frigid Tharsis plateau. ROCKE-3D
636 does not have a land ice or glacier parameterization that could simulate the eventual flow of these
637 glaciers and determine how glacial melt could recharge the system. But regardless, the planet is
638 left with comparatively little water in the active hydrological cycle. We find planetary obliquity
639 is key to determining where precipitation falls as rain or snow in these simulations. Simulations
640 with 0° obliquity produce greater rainfall near locations with valley network formations.
641 Simulations with 45° obliquity are slightly cooler than those with either modern or 0° obliquity
642 and have rainfall patterns that are inconsistent with the geologic evidence for fluvial activity on
643 Noachian Mars. Note our simulations do not include the physics of CO₂ condensation. But
644 importantly, many of our simulations that included H₂ had surface temperatures remain above the
645 CO₂ condensation temperature, regardless of obliquity.

646 The timing of the formation of Tharsis relative to the valley network formations is critical
647 to understanding the climatic conditions under which they formed. Simulations using a plausible
648 paleotopography (see Bouley et al. [2016]) have increased amounts of precipitation globally due
649 to the lack of Tharsis acting as a cold trap for snow and ice. Again, simulations with modern or
650 0° obliquity are more consistent with rainfall over locations with valley network formations than
651 45° obliquity.

652 If Noachian Mars had oceans (following Tharsis emplacement with modern topography),
653 the most plausible locations for those oceans in the northern hemisphere lowlands and Hellas basin

654 are inefficient for meridional heat transport. The global climate is no warmer when an ocean is
655 present than when it is absent, assuming the background atmospheric composition is supportive of
656 surface liquid water already. The presence of oceans does alter precipitation patterns, however,
657 and precipitation and rainfall are increased over much of the planet. A Hellas ocean in particular
658 produces increased rainfall in many locations where valley network formations and paleolakes are
659 seen in the modern surface geology.

660

661 ACKNOWLEDGEMENTS

662 Guzewich, Way, Del Genio, Aleinov, Wolf, and Tsigaridis were supported by the NASA Nexus
663 for Exoplanet System Science program that helped develop the ROCKE-3D GCM. We thank
664 Bouley et al. (2016) for helpfully including the paleotopographic file in their supplemental material
665 to make some of these simulations plausible. Model input and boundary condition files, rundecks
666 (simulation setup files), and final output files are available here: .

667

668 REFERENCES

669

670 Abramopoulos, F., Rosenzweig, C., & Choudhury, B. (1988). Improved Ground Hydrology
671 Calculations for Global Climate Models (GCMs): Soil Water Movement and Evapotranspiration,
672 *Journal of Climate*, 1(9), 921-941. doi:10.1175/1520-0442(1988)001<0921:IGHCFG>2.0.CO;2

673

674 Batalha, N., S.D. Domagal-Goldman, R. Ramirez and J.F. Kasting (2015), Testing the early
675 Mars H₂-CO₂ greenhouse hypothesis with a 1-D photochemical model, *Icarus*, 258, 337-349,
676 <https://doi.org/10.1016/j.icarus.2015.06.016>.

677

678 Bouley, S., Baratoux, D., Matsuyama, I. *et al* (2016). Late Tharsis formation and implications for
679 early Mars, *Nature* 531, 344–34, <https://doi.org/10.1038/nature17171>.

680

681 Bouley, S., Baratoux, D., Paulien, N., Missenard, Y., Saint-Bézar, B. (2017), The revised
682 tectonic history of Tharsis, *Earth and Planetary Science Letters*, 488, 126-133,
683 <https://doi.org/10.1016/j.epsl.2018.02.019>.

684
685 Bryne, B., and C. Goldblatt (2015), Diminished greenhouse warming from Archean methane due
686 to solar absorption lines, *Climate of the Past*, 11, 559-570, doi:10.5194/cp-11-559-2015.
687
688 Cassata, W., D.L. Schuster, P.R. Renne, and B.P. Weiss (2012), Trapped Ar isotopes in
689 meteorite ALH 84001 indicate Mars did not have a thick ancient atmosphere. *Icarus*, 221, 461–
690 465, <https://doi.org/10.1016/j.icarus.2012.05.005>.
691
692 Carr, M. H. (1996), *Water on Mars*, 229 pp., Oxford Univ. Press, New York.
693
694 Carter, J., Poulet, F., Bibring, J.-P., Mangold, N., and Murchie, S. (2013), Hydrous minerals on
695 Mars as seen by the CRISM and OMEGA imaging spectrometers: Updated global view, *J.*
696 *Geophys. Res. Planets*, 118, 831– 858, doi: 10.1029/2012JE004145.
697
698 Cassanelli JP, Head JW III (2015), Firm densification in a Late Noachian “icy highlands” Mars:
699 implications for ice sheet evolution and thermal response, *Icarus* 253:243–55,
700 <https://doi.org/10.1016/j.icarus.2015.03.004>.
701
702 Claire, M.W., Sheets, J., Cohen, M., Ribas, I., Meadows, V.S., & Catling, D. (2012) “The
703 Evolution of Solar Flux From 0.1 nm to 160 μm: Quantitative Estimates for Planetary Studies.”
704 *The Astrophysical Journal* 757:95 (12pp)
705
706 Clancy, R., A. W. Grossman, M. J. Wolff, P. B. James, D. J. Rudy, Y. N. Billawala, B. J. Sandor,
707 S. W. Lee, and D. O. Muhleman(1996), Water vapor saturation at low altitudes around Mars
708 aphelion: A key to Mars climate, *Icarus*, 122, 36–62, <https://doi.org/10.1006/icar.1996.0108>.
709
710 Clough, S. A., Shephard, M. W., Mlawer, E. J., Delamre, J. S., Iacono, M. J., Cady-Pereira, K.,
711 Boukabara, S., and Brown, P. D. (2005), Atmospheric radiative transfer modeling: a summary of
712 the AER codes. *J. Quant. Spec. Rad. Trans.* 91, 233-244. doi:10.1016/j.jqsrt.2004.05.058
713
714 Di Achille, G. and B.M. Hynek (2010), Ancient ocean on Mars supported by global distribution
715 of deltas and valleys, *Nature Geoscience*, 3, 459–463, <https://doi.org/10.1038/ngeo891>.
716
717 Ehlmann, B., Mustard, J., Murchie, S. *et al.* Subsurface water and clay mineral formation during
718 the early history of Mars. *Nature* 479, 53–60 (2011). <https://doi.org/10.1038/nature10582>.
719
720 Fassett, C. I., and Head, J. W. (2005), Fluvial sedimentary deposits on Mars: Ancient deltas in
721 a crater lake in the Nili Fossae region, *Geophys. Res. Lett.*, 32, L14201,
722 doi:10.1029/2005GL023456.
723

724 Fastook JL, Head JW III, Marchant DR, Forget F, Madeleine JB (2012), Early Mars climate near
725 the Noachian–Hesperian boundary: independent evidence for cold conditions from basal melting
726 of the south polar ice sheet (Dorsa Argentea formation) and implications for valley network
727 formation. *Icarus* 219:25–40, <https://doi.org/10.1016/j.icarus.2012.02.013>.
728

729 Fastook JL, Head JW III (2014), Glaciation in the Late Noachian icy highlands: ice
730 accumulation, distribution, flow rates, basal melting, and top-down melting rates and
731 patterns, *Planet. Space Sci.* 106:82–98, <https://doi.org/10.1016/j.pss.2014.11.028>.
732

733 Forget, F., and R. Pierrehumbert (1997), Warming Early Mars with Carbon Dioxide Clouds That
734 Scatter Infrared Radiation, *Science*, 278, 5341, 1273-1276, DOI:
735 10.1126/science.278.5341.1273.
736

737 Forget, F., et al. (2013), 3D modelling of the early martian climate under a denser CO₂
738 atmosphere: Temperatures and CO₂ ice clouds, *Icarus*, 222(1), 81-99,
739 <https://doi.org/10.1016/j.icarus.2012.10.019>.
740

741 Godin, P. J., Ramirez, R. M., Campbell, C. L., Wizenberg, T., Nguyen, T. G., Strong, K. and
742 Moores, J. E. (2020) Collision-Induced Absorption of CH₄-CO₂ and H₂-CO₂ Complexes and
743 Their Effect on the Ancient Martian Atmosphere. *J. Geophys. Res. Planets.*, 125, 12,
744 e2019JE006357. <https://doi.org/10.1029/2019JE006357>
745

746 Gough, D.O. (1981) “Solar Interior Structure and Luminosity Variations.” *Solar Physics* 74, 21-
747 34
748

749 Grant, J. A., Wilson, S. A., Mangold, N., Calef, F., and Grotzinger, J. P. (2014), The timing of
750 alluvial activity in Gale crater, Mars, *Geophys. Res. Lett.*, 41, 1142– 1148,
751 doi:10.1002/2013GL058909.
752

753 Grotzinger, J.P. et al., (2014), A Habitable Fluvio-Lacustrine Environment at Yellowknife Bay,
754 Gale Crater, Mars, *Science*, 343, 6169, DOI: 10.1126/science.1242777.
755

756 Haberle, R. M., Zahnle, K., Barlow, N. G., & Steakley, K. E. (2019). Impact degassing of H₂
757 on early mars and its effect on the climate system. *Geophysical Research Letters*, 46, 13355–
758 13362. <https://doi.org/10.1029/2019GL084733>.
759

760 Hansen, J., G. Russell, D. Rind, P. Stone, A. Lacis, S. Lebedeff, R. Ruedy, and L. Travis, 1983:
761 Efficient three-dimensional global models for climate studies: Models I and II. *Mon. Weather*
762 *Rev.*, 111, 609-662, doi:10.1175/1520-0493(1983)111<0609:ETDGMF>2.0.CO;2.
763

764 Hayworth, B.P.C., R.K. Kopparapu, J. Haqq-Misra et al. (2020), Warming early Mars with
765 climate cycling: The effect of CO₂-H₂ collision-induced absorption, *Icarus*, 345,
766 <https://doi.org/10.1016/j.icarus.2020.113770>.
767

768 Hirschmann MM, Withers AC. (2008), Ventilation of CO₂ from a reduced mantle and
769 consequences for the early Martian greenhouse, *Earth Planet. Sci. Lett.* 270:147–55,
770 <https://doi.org/10.1016/j.epsl.2008.03.034>.
771

772 Hurowitz, J.A., Fischer, W.W., Tosca, N.J. and Milliken, R.E., 2010. Origin of acidic surface
773 waters and the evolution of atmospheric chemistry on early Mars. *Nature Geoscience*, 3(5),
774 pp.323-326.
775

776 Hynek, B.M. and R.J. Phillips (2001), Evidence for Extensive Denudation of the Martian
777 Highlands, *Geology*, 21(5), 407-410, [https://doi.org/10.1130/0091-](https://doi.org/10.1130/0091-7613(2001)029<0407:EFEDOT>2.0.CO;2)
778 [7613\(2001\)029<0407:EFEDOT>2.0.CO;2](https://doi.org/10.1130/0091-7613(2001)029<0407:EFEDOT>2.0.CO;2).
779

780 Hynek, B. M., Beach, M., and Hoke, M. R. T. (2010), Updated global map of Martian valley
781 networks and implications for climate and hydrologic processes, *J. Geophys. Res.*, 115, E09008,
782 [doi:10.1029/2009JE003548](https://doi.org/10.1029/2009JE003548).
783

784 Irwin, R. P., Howard, A. D., Craddock, R. A., and Moore, J. M. (2005), An intense terminal
785 epoch of widespread fluvial activity on early Mars: 2. Increased runoff and paleolake
786 development, *J. Geophys. Res.*, 110, E12S15, [doi:10.1029/2005JE002460](https://doi.org/10.1029/2005JE002460).
787

788 Jakosky, B.M. et al. (2018), Loss of the Martian atmosphere to space: Present-day loss rates
789 determined from MAVEN observations and integrated loss through time, *Icarus*, 315, 146-157,
790 [doi: 10.1016/j.icarus.2018.05.030](https://doi.org/10.1016/j.icarus.2018.05.030).
791

792 Kamada, A., T. Kuroda, Y. Kasaba, N. Terada, H. Nakagawa, and K. Toriumi (2020), A coupled
793 atmosphere-hydrosphere climate model of early Mars: A ‘cool and wet’ scenario for the
794 formation of water channels, *Icarus*, 338, 113567, <https://doi.org/10.1016/j.icarus.2019.113567>.
795

796 Kasting, J.F. (1991), CO₂ Condensation and the Climate of Early Mars, *Icarus*, 94(1), 1-13,
797 [https://doi.org/10.1016/0019-1035\(91\)90137-I](https://doi.org/10.1016/0019-1035(91)90137-I).
798

799 Kasting, J.F. (1997), Warming Early Earth and Mars, *Science*, 279, 5316, DOI:
800 [10.1126/science.276.5316.1213](https://doi.org/10.1126/science.276.5316.1213).
801

802 Kerber, L., F. Forget, and R.D. Wordsworth (2015), Sulfur in the early martian atmosphere
803 revisited: Experiments with a 3-D Global Climate Model, *Icarus*, 261, 133-148,
804 <https://doi.org/10.1016/j.icarus.2015.08.011>.

805
806 Kite, E. S., Williams, J.-P., Lucas, A., & Aharonson, O. (2014). Low palaeopressure of the
807 martian atmosphere estimated from the size distribution of ancient craters. *Nature Geoscience*, 7,
808 335–339, <https://doi.org/10.1038/ngeo2137>.
809
810 Kite, E. S., Sneed, J., Mayer, D. P., and Wilson, S. A. (2017), Persistent or repeated surface
811 habitability on Mars during the late Hesperian - Amazonian, *Geophys. Res. Lett.*, 44, 3991–
812 3999, doi:10.1002/2017GL072660.
813
814 Kopparapu, R. K., Ramirez, R., Kasting, J.F., Eymet, V., Robinson, T.D., Mahadevan, S.,
815 Terrien, R.C., Domagal-Goldman, S., Meadows, V., and Deshpande, R. (2013) “Habitable
816 Zones Around Main-Sequence Stars: New Estimates.” *The Astrophysical Journal*
817 765:131(16pp)

818 Kuhn, W. R., and S. K. Atreya, Ammonia photolysis and the greenhouse effect in the primordial
819 atmosphere of the Earth, *Icarus*, 37, 207-213, 1979, [https://doi.org/10.1016/0019-](https://doi.org/10.1016/0019-1035(79)90126-X)
820 1035(79)90126-X.

821 Lean, J., Beer, J. and Bradley, S. (1995) “Reconstruction of solar irradiance since 1610:
822 Implications for climate change.” *Geophys. Res. Lett.* 22, 3195-3198
823
824 Manga, M., Patel, A., Dufek, J., and Kite, E. S. (2012), Wet surface and dense atmosphere on
825 early Mars suggested by the bomb sag at Home Plate, Mars, *Geophys. Res. Lett.*, 39, L01202,
826 doi:10.1029/2011GL050192.
827
828 Matsuyama, I. & Manga, M. (2010), Mars without the equilibrium rotational figure, Tharsis, and
829 the remnant rotational figure. *J. Geophys. Res.* 115, E12020.
830
831 Masursky, H. (1973), An overview of geological results from Mariner 9, *J. Geophys. Res.*, 78(
832 20), 4009–4030, doi:10.1029/JB078i020p04009.
833
834 Mischna, M. A., Baker, V., Milliken, R., Richardson, M., and Lee, C. (2013), Effects of
835 obliquity and water vapor/trace gas greenhouses in the early martian climate, *J. Geophys. Res.*
836 *Planets*, 118, 560–576, doi:10.1002/jgre.20054.
837 Murchie, S., et al. (2009), Evidence for the origin of layered deposits in Candor Chasma, Mars,
838 from mineral composition and hydrologic modeling, *J. Geophys. Res.*, 114, E00D05,
839 doi:10.1029/2009JE003343.
840
841 Mondelain, D., C. Boulet, and J.-M. Hartmann (2021), The binary absorption coefficients for H₂
842 + CO₂ mixtures in the 2.12–2.35 μm spectral region determined by CRDS and by semi-empirical

843 calculations, *Journal of Quantitative Spectroscopy and Radiative Transfer*, 260, 107454,
844 <https://doi.org/10.1016/j.jqsrt.2020.107454>.
845
846 Navarro, T., Madeleine, J.-B, Forget, F., Spiga, A., Millour, E., Montmessin, F., and Määttänen,
847 A. (2014), Global climate modeling of the Martian water cycle with improved microphysics and
848 radiatively active water ice clouds, *J. Geophys. Res. Planets*, 119, 1479– 1495,
849 doi:10.1002/2013JE004550.
850
851 Palumbo, A. M., & Head, J. W. (2018). Early Mars climate history: Characterizing a “warm
852 and wet” Martian climate with a 3-D global climate model and testing geological predictions.
853 *Geophysical Research Letters*, 45, 10,249– 10,258. <https://doi.org/10.1029/2018GL079767>.
854
855 Palumbo, A.M., J.W. Head, and L. Wilson (2020), Rainfall on Noachian Mars: Nature, timing,
856 and influence on geologic processes and climate history, *Icarus*, 347, 113782,
857 <https://doi.org/10.1016/j.icarus.2020.113782>.
858
859 Perron, J. T., Mitrovica, J. X., Manga, M., Matsuyama, I. & Richards, M. A., (2007) Evidence
860 for an ancient martian ocean in the topography of deformed shorelines. *Nature*, 447, 840–843.
861
862 Pieri, D.C. (1981), Martian Valleys: Morphology, Distribution, Age, and Origin, *Science*, 210,
863 4472, 895-897, DOI: 10.1126/science.210.4472.895.
864
865 Pollack, J.B. (1979), Climate Change on the Terrestrial Planets, *Icarus*, 37, 479-553,
866 [https://doi.org/10.1016/0019-1035\(79\)90012-5](https://doi.org/10.1016/0019-1035(79)90012-5).
867
868 Pollack, J. B., J. F. Kasting, S. M. Richardson, and K. Poliakoff (1987), The case for a wet,
869 warm climate on early Mars, *Icarus* 71, 203-224, [https://doi.org/10.1016/0019-1035\(87\)90147-3](https://doi.org/10.1016/0019-1035(87)90147-3).
870
871 Postawko, S. E., and Kuhn, W. R. (1986), Effect of the greenhouse gases (CO₂, H₂O, SO₂) on
872 Martian paleoclimate, *J. Geophys. Res.*, 91(B4), 431– 438, doi:10.1029/JB091iB04p0D431.
873
874 Ramirez, R., Kopparapu, R., Zuger, M. *et al.* Warming early Mars with CO₂ and H₂.*Nature*
875 *Geosci* 7, 59–63 (2014). <https://doi.org/10.1038/ngeo2000>.
876
877 Ramirez, R.M., Craddock, R.A., and Usui, T. (2020), Climate Simulations for Early Mars with
878 Estimated Precipitation, Runoff, and Erosion Rates, *J. Geophys. Res. Planets*, 125,
879 e2019JE006160, <https://doi.org/10.1029/2019JE006160>.
880
881 Roe, H.G., (2012), Titan’s Methane Weather, *Annual Review of Earth and Planetary Science*,
882 40:355-82, doi:10.1146/annurev-earth-040809-152548.
883

884 Rosenzweig, C., & Abramopoulos, F. (1997). Land-Surface Model Development for the GISS
885 GCM, *Journal of Climate*, 10(8), 2040-2054. doi:10.1175/1520-
886 0442(1997)010<2040:LSMDFT>2.0.CO;2
887
888 Schon, S. C., J. W. Head, and C. I. Fassett (2012), An overfilled lacustrine system and
889 progradational delta in Jezero crater, Mars: Implications for Noachian climate, *Planet. Space*
890 *Sci.*, 67, 28–45, doi:10.1016/j.pss.2012.02.003.
891
892 Soto, A., M. I. Richardson, and C. E. Newman (2010), Global constraints on rainfall on ancient
893 Mars: Oceans, lakes, and valley networks, *Lunar Planet. Sci.*, , *XLI*, Abstract 2397.
894
895 Tarnas, J.D., Mustard, J.F., Lollar, B.S., Bramble, M.S., Cannon, K.M., Palumbo, A.M. and
896 Plesa, A.C., 2018. Radiolytic H₂ production on Noachian Mars: Implications for habitability and
897 atmospheric warming. *Earth and Planetary Science Letters*, 502, pp.133-145.
898 Tian F, Claire MW, Haqq-Misra JD, Smith M, Crisp DC, et al. (2010), Photochemical and
899 climate consequences of sulfur outgassing on early Mars. *Earth Planet. Sci. Lett.* 295: 412–18,
900 <https://doi.org/10.1016/j.epsl.2010.04.016>.
901
902 Tosca, N.J., Ahmed, I.A., Tutolo, B.M., Ashpittel, A. and Hurowitz, J.A., 2018. Magnetite
903 authigenesis and the warming of early Mars. *Nature geoscience*, 11(9), pp.635-639.
904
905 Turbet, M., Gillmann, C., Forget, F., Baudin, B., Palumbo, A., Head, J. and Karatekin, O. (2020)
906 The environmental effects of very larger bolide impacts on early Mars explored with a hierarchy
907 of numerical models. *Icarus*, 335, 113419. <https://doi.org/10.1016/j.icarus.2019.113419>
908
909 Turbet, M., C. Boulet, and T. Karman (2020b), Measurements and semi-empirical calculations of
910 CO₂ + CH₄ and CO₂ + H₂ collision-induced absorption across a wide range of wavelengths and
911 temperatures. Application for the prediction of early Mars surface temperature, *Icarus*, in press,
912 <https://doi.org/10.1016/j.icarus.2020.113762>
913
914 Urata, R. A. and Toon, O. B. (2013), Simulations of the martian hydrologic cycle with a general
915 circulation model: Implications for the ancient martian climate, *Icarus*, 226, 229-250.
916 <http://dx.doi.org/10.1016/j.icarus.2013.05.014>
917
918 Warren, A. O., Kite, E. S., Williams, J.-P., & Horgan, B. (2019). Through the thick and thin:
919 New constraints on Mars paleopressure history 3.8 - 4 Ga from small exhumed craters. *Journal*
920 *of Geophysical Research: Planets*, 124, 2793– 2818. <https://doi.org/10.1029/2019JE006178>.
921
922 Way, M.J., A.D. Del Genio, N.Y. Kiang, L.E. Sohl, D.H. Grinspoon, I. Aleinov, M. Kelley, and
923 T. Clune, 2016: Was Venus the first habitable world of our solar system? *Geophys. Res. Lett.*,
924 **43**, no. 16, 8376-8383, doi:10.1002/2016GL069790.

925
926 Way, M.J., I. Aleinov, D.S. Amundsen, M.A. Chandler, T. Clune, A.D. Del Genio, Y. Fujii, M.
927 Kelley, N.Y. Kiang, L. Sohl, and K. Tsigaridis, 2017: Resolving Orbital and Climate Keys of
928 Earth and Extraterrestrial Environments with Dynamics 1.0: A general circulation model for
929 simulating the climates of rocky planets. *Astrophys. J. Supp. Series*, **231**, no. 1, 12,
930 doi:10.3847/1538-4365/aa7a06.
931
932 Way, M.J., A.D. Del Genio, I. Aleinov, T.L., Clune, M. Kelley, N.Y. Kiang, 2018: Climates of
933 Warm Earth-like Planets I 3D Model Simulations. *Astrophys. J. Supp. Series*, 239, 24
934 doi:10.3847/1538-4365/aae9e1
935
936 Way, M.J., and A.D. Del Genio, 2020: Venusian habitable climate scenarios: Modeling Venus
937 through time and applications to slowly rotating Venus-like exoplanets. *J. Geophys. Res.:*
938 *Planets*, 125, e2019JE006276. doi:10.1029/2019JE006276
939
940 Williams, R.M.E. et al. (2013), Martian Fluvial Conglomerates at Gale Crater, *Science*, 340,
941 6136, 1068-1072, DOI: 10.1126/science.1237317.
942
943 Wolf, E. T. and Toon, O. B. (2013), Hospitable archean climates simulated by a general
944 circulation model, *Astrobiology*, 13, 656–673, doi:10.1089/ast.2012.0936.
945
946 Wordsworth, R., Forget, F., and Eymet, V. (2010) “Infrared collision-induced and far-line
947 absorption in dense CO₂ atmospheres.” *Icarus* 210, 992-997
948
949 Wordsworth R, Pierrehumbert R (2013), Hydrogen-nitrogen greenhouse warming in Earth's
950 early atmosphere. *Science* 339:64–67, DOI: 10.1126/science.1225759.
951
952 Wordsworth R, Forget F, Millour E, Head JW, Madeleine JB, Charnay B. (2013), Global
953 modelling of the early martian climate under a denser CO₂ atmosphere: water cycle and ice
954 evolution, *Icarus* 222:1–19, <https://doi.org/10.1016/j.icarus.2012.09.036>.
955
956 Wordsworth, R. (2015), Atmospheric heat redistribution and collapse on tidally locked rocky
957 planets. *The Astrophysical Journal*, 806(2), p.180.
958
959 Wordsworth, R. D., Kerber, L., Pierrehumbert, R. T., Forget, F., and Head, J. W. (2015),
960 Comparison of “warm and wet” and “cold and icy” scenarios for early Mars in a 3-D climate
961 model, *J. Geophys. Res. Planets*, 120, 1201– 1219. doi:10.1002/2015JE004787.
962
963 Wordsworth, R.D. (2016), The Climate of Early Mars, *Annual Review of Earth and Planetary*
964 *Science*, 44, 381-408, <https://doi.org/10.1146/annurev-earth-060115-012355>.
965

966 Wordsworth, R.D., Kalugina, Y., Lokshantov, S., Vigasin, A., Ehlmann, B., Head, J.,
967 Sanders, C., and Wang, H. (2017), Transient reducing greenhouse warming on early Mars,
968 *Geophys. Res. Lett.*, 44, 665– 671, doi:[10.1002/2016GL071766](https://doi.org/10.1002/2016GL071766).
969
970 Yang, J., Leconte, J., Wolf, E.T., Goldblatt, C., Feldl, N., Merlis, T., Wang, Y, Koll, D.D.B.,
971 Ding, F., Forget, F. and Abbot, D.S. (2016) “Differences in Water Vapor Radiative Transfer
972 Among 1D Models Can Significantly Affect the Inner Edge of the Habitable Zone.”
973 *The Astrophysical Journal*, 826:222 (11pp)
974
975
976
977
978